

Abundances of neutron-capture elements in stars of the galactic disk substructures ★ ★★

T.V. Mishenina^{1,2}, M. Pignatari³, S.A. Korotin¹, C. Soubiran², C. Charbonnel^{4,5}, F.-K. Thielemann³, T.I. Gorbaneva¹, and N.Yu. Basak¹

¹ Astronomical Observatory, Odessa National University, and Isaac Newton Institute of Chile, Odessa Branch, T.G.Shevchenko Park, Odessa 65014 Ukraine,
email:tamar@deneb1.odessa.ua

² Université de Bordeaux 1 - CNRS - Laboratoire d'Astrophysique de Bordeaux, UMR 5804, BP 89, 33271 Floirac Cedex, France,
email:Caroline.Soubiran@obs.u-bordeaux1.fr

³ Department of Physics, University of Basel, Klingelbergstrabe 82, 4056 Basel, Switzerland
email:marco.pignatari@unibas.ch

⁴ Geneva Observatory, University of Geneva, 1290 Versoix, Switzerland

⁵ IRAP, UMR 5277 CNRS and Université de Toulouse, 31400 Toulouse, France

ABSTRACT

Aims. The aim of this work is to present and discuss the observations of the iron peak (Fe, Ni) and neutron-capture element (Y, Zr, Ba, La, Ce, Nd, Sm, and Eu) abundances for 276 FGK dwarfs, located in the galactic disk with metallicity $-1 < [\text{Fe}/\text{H}] < +0.3$.

Methods. Atmospheric parameters and chemical composition of the studied stars were determined from an high resolution, high signal-to-noise echelle spectra obtained with the echelle spectrograph ELODIE at the Observatoire de Haute-Provence (France). Effective temperatures were estimated by the line depth ratio method and from the H_α line-wing fitting. Surface gravities ($\log g$) were determined by parallaxes and the ionization balance of iron. Abundance determinations were carried out using the LTE approach, taking the hyperfine structure for Eu into account, and the abundance of Ba was computed under the NLTE approximation.

Results. We are able to assign most of the stars in our sample to the substructures of the Galaxy thick disk, thin disk, or Hercules stream according to their kinematics. The classification of 27 stars is uncertain. For most of the stars in the sample, the abundances of neutron-capture elements have not been measured earlier. For all of them, we provide the chemical composition and discuss the contribution from different nucleosynthesis processes.

Conclusions.

The $[\text{Ni}/\text{Fe}]$ ratio shows a flat value close to the solar one for the whole metallicity range, with a small scatter, pointing to a nearly solar Ni/Fe ratio for the ejecta of both core-collapse SN and SNIa. The increase in the $[\text{Ni}/\text{Fe}]$ for metallicity higher than solar is confirmed, and it is due to the metallicity dependence of ^{56}Ni ejecta from SNIa. Under large uncertainty in the age determination of observed stars, we verified that there is a large dispersion in the AMR in the thin disk, and no clear trend as in the thick disk. That may be one of the main reasons for the dispersion, observed for the *s*-process elements in the thin disk (e.g., Ba and La), whereas much narrower dispersion can be seen for *r*-process elements (e.g., Eu). Within the current uncertainties, we do not see a clear decreasing trend of $[\text{Ba}/\text{Fe}]$ or $[\text{La}/\text{Fe}]$ with metallicity in the thin disk, except maybe for super-solar metallicities. We cannot confirm an increase in the mentioned ratios with decreasing stellar age.

Key words. Nucleosynthesis – Stars: abundances – Stars: late-type – Galaxy: evolution

1. Introduction

The chemical abundances that we observe today in the solar system and in stars provide fundamental constraints in our understanding of the stellar evolution and nucleosynthesis, of the galactic formation and chemical evolution, and of the near-field cosmology observations. In particular, despite their low abundance, elements heavier than iron have been observed over a large sample of stars, spreading over Gyrs in age and over orders of magnitude in metal content, in our Galaxy, and in more distant objects (e.g., Sneden et al. 2008; Tolstoy et al. 2009 and reference therein). Most of their abundances are produced by neutron capture processes: the slow neutron capture (or the *s*-

process) and the rapid neutron capture process (or the *r*-process) (Burbidge et al. 1957; Cameron 1957).

The first phenomenological studies introduced three different components for the *s*-process (e.g., Käppeler et al. 1989): the weak *s*-process component, producing most of the *s*-species between Fe and Sr; the main *s*-process component for abundances between Sr and Pb; and the strong *s*-process component, responsible for the production of 50 % of the solar ^{208}Pb . Full nucleosynthesis simulations based on realistic stellar models mostly confirm this scenario. The bulk of the weak *s*-process component is made in massive stars, triggered by the activation of the $^{22}\text{Ne}(\alpha, \text{n})^{25}\text{Mg}$ reaction in the convective He-burning core and in the following convective C-burning shell (e.g., Rauscher et al. 2002; The et al. 2007; Pignatari et al. 2010). The main and strong *s*-process components are produced in the AGB stars at the solar-like and low metallicity, respectively (e.g., Gallino et al. 1998; Bisterzo et al. 2011). Most of the neutrons are provided by the $^{13}\text{C}(\alpha, \text{n})^{16}\text{O}$ reaction in the radiative ^{13}C -pocket

* Based on spectra collected with the ELODIE spectrograph at the 1.93-m telescope of the Observatoire de Haute Provence (France).

** Tables 4 and 5 are only available in electronic form at the CDS via the anonymous ftp to cdsarc.u-strasbg.fr (130.79.128.5) or via [http://cdsweb.u-strasbg.fr/cgi-bin/qcat?J/A+A/\(vol\)/\(page\)](http://cdsweb.u-strasbg.fr/cgi-bin/qcat?J/A+A/(vol)/(page))

formed right after the third dredged-up event Straniero et al. 2003, with a relevant contribution from the partial activation of the $^{22}\text{Ne}(\alpha, \text{n})^{25}\text{Mg}$ in the convective thermal pulse (Gallino et al. 1998). In particular, the Galactic chemical evolution (GCE) computations confirmed that different generations of the AGB stars have to be taken into account to properly study the *s*-process distribution of the solar system (Travaglio et al. 2004; Serminato et al. 2009).

The origin of heavy *r*-process elements remains uncertain. At least three sources have been proposed, namely: 1) the neutrino-induced winds from the core-collapse supernovae (e.g., Woosley et al. 1994); 2) the enriched neutron-rich matter from merging neutron stars (e.g., Freiburghaus et al. 1999), and/or neutron-star/black hole mergers (Surman et al. 2008); 3) polar jets from rotating MHD core-collapse supernova (Nishimura et al. 2006). For a more detailed description of different *r*-process scenarios, we refer to Thielemann et al. (2011). For the recent results related to the *r*-process, we refer to Winteler et al. (2012) and Korobkin et al. (2012).

The surface abundances of the FGK dwarf stars do not show any noticeable change due to the stellar evolution, reflecting their pristine chemical composition. Stars in the range of metallicity $-1 < [\text{Fe}/\text{H}] < +0.3$ dex were born in the interstellar medium, which had been enriched by several generations of stars. Those stars do not have homogeneous kinematics, and were possibly formed in different galactic subsystems or were captured from outside of the Galaxy (Feltzing et al. 2009; Marsakov & Borkova 2005; Klochkova et al. 2011). The analysis of their main features may be a powerful tool for tracing the formation of the galactic substructure and the galactic chemical enrichment.

According to Gilmore & Reid (1983), the stellar distribution from the galactic plane towards the southern galactic pole is described by two exponentials with different height and density, introducing the concept of the *thick disk*. In the past decades, it has been shown that the stars of the thick disk and the *thin disk* have different kinematics, ages, and the abundances of α -elements. The behavior of the neutron-capture elements relative to metallicity and the study of the *s*- and *r*-process contributions for those two substructures were presented by different authors (Prochaska et al. 2000; Mashonkina & Gehren 2000, 2001; Mashonkina et al. 2004; Alende Prieto et al. 2004; Brewer & Carney 2006; Bensby et al. 2005; Reddy et al. 2006; Nissen & Shuster 2008; Felting et al. 2009; etc.).

The galactic disk also includes stellar clusters and groups of stars with their peculiar motion. Among them is the Hercules stream, first investigated in detail by Eggen (1958), and then by Fux (2001), Famaey et al. (2005). According to Famaey et al. (2005) the Hercules stream has dynamical origin and can be made of stars with very different birth locations and ages. Thus, no coherent chemical trend is expected for them, and on the contrary, a large dispersion of their properties should be observed. Kinematically, the Hercules stream is somewhere between the thin disk and the thick disk and complicates their separation. When performing the deconvolution of the thin and the thick disks on kinematical criteria, it is important to consider that group of stars to obtain pure samples. In the papers by Soubiran & Girard (2005), Bensby et al. (2007), and Pakhomov (2011) the chemical composition and kinematics of the stars was studied. The work by Soubiran & Girard (2005) shows that those stars are chemically closer to the thin disk, but according to Bensby et al. (2007) and Pakhomov (2011), the stars represent a mixture of stars of the thick and thin disks.

The accuracy of determining of the element abundances, parameters of the thick and thin disks, stellar ages, as well as the

criteria for the star's assignments to different substructures, play important roles in interpreting the observational data. One of the reliable ways of investigating the formation and evolution of different structures of the disk is to study the chemical composition of the stars belonging to those structures in detail. Thus, theoretical stellar abundance yields can be used to investigate how the Galactic substructures and the Galaxy as a whole have evolved up to the present stage.

The goal of the present work is to provide and analyze the abundance signature of Ni and the neutron-capture elements for 276 dwarfs in the solar neighborhood in the metallicity range $-1 < [\text{Fe}/\text{H}] < 0.3$. The paper is structured as follows. The observations, processing, and selection of stars are described in Section 2. The atmospheric parameters, the abundance determinations for Y, Zr, Ba, La, Ce, Nd, Sm, and Eu, and the error analysis are presented in Sections 3, 4, and 5, respectively. In Section 6, the final results are given and discussed. Conclusions are drawn in Section 7.

2. Observations, processing, and selection of stars

This study is a part of a wider project, in which the metallicity distribution and behavior of some elements in the local thin disk are investigated for a complete sample of the G and K dwarfs and giants in the solar neighborhood (Mishenina et al. 2004, 2006, 2008). The transition between the thin and thick disks in kinematics and abundance trends (Mishenina et al. 2004), the vertical distribution of the Galactic disk, the measurement of its surface mass density (Bienaymé et al. 2006), its age metallicity relation (AMR) and age velocity relation (AVR) (Soubiran et al. 2008), as well as the construction of the chemical evolution model (Nikityuk & Mishenina 2006) - all of those were studied on the basis of the collection of the above - mentioned data. In the present paper, we have considered the neutron-capture elements for the entire set of dwarfs in our example. Following the approach in which the kinematical and chemical information is combined, the G and K dwarfs within 25 pc from the Sun were selected from the Hipparcos catalog: for this study we analyzed the spectra of 276 stars (F-G-K V) with metallicities in the range $-1 < [\text{Fe}/\text{H}] < +0.3$. The spectra were obtained in the wavelength region $\lambda 4400 - 6800 \text{ \AA}$ and with the signal-to-noise ratios (*S/N*) of about 100-350, using the 1.93 m telescope at the Observatoire de Haute-Provence (OHP, France) equipped with the echelle-spectrograph ELODIE (Baranne et al. 1996), which provides the resolving power of $R = 42000$.

The complex preprocessing of the images is available online, and it allows the spectroscopic data to be obtained in digital form with the radial velocity V_r (Katz et al. 1998) immediately after the exposure. The spectra have been treated to correct the blaze efficiency and cosmic and telluric lines following Katz et al. (1998). The subsequent processing of the studied spectra (including the continuous spectrum level set up, the development of the dispersion curve, the measurement of equivalent widths, etc.) was performed by us with the DECH20 software package (Galazutdinov 1992). The equivalent widths (EWs) of the spectral lines were measured by the Gaussian profile fitting.

Specific features were used to select the stars that belong to the thin and thick disks or to other galactic substructures. Those include the spatial distribution and local density of stars, space velocity, metallicity, and age. Since the velocity distribution is well studied for those substructures, we applied the kinematic approach for separating the stars, determining the probability that each star is a member of the thin or thick disks or of the

Hercules stream, based on its spatial velocity, kinematic parameters of the disks, and the stream, as well as the percentage of the stars of the studied sample in each disk, and in the Hercules stream. The probability of each star belonging to the thin or thick disks or to the Hercules stream was computed using the (U, V, W) velocities by the method of Soubiran & Girard (2005) with parallaxes and the proper motion from van Leeuwen (2007). In our sample (276 stars), 21 stars belong to the thick disk, 212 to the thin disk, 16 to the Hercules stream, and 27 are unclassified. The probabilities stars are classified by their belonging to the thick and thin disks or to the Hercules stream are presented in Table 4.

3. Atmospheric parameters

The atmospheric parameters for the target stars were determined in our previous studies (Mishenina & Kovtyukh 2001; Mishenina et al. 2004; Mishenina et al. 2008). The effective temperatures T_{eff} were estimated by calibrating the ratio of the central depths of the lines with different potentials of the lower level developed by Kovtyukh et al. (2004). For metal-poor stars the effective temperatures were determined from the H_{α} line-wing fitting (Mishenina & Kovtyukh 2001). The surface gravities $\log g$ were computed by two methods. For the stars with T_{eff} higher than 5000 K by the iron ionization balance and the parallax, the parallax was the only method used for the cooler stars. The microturbulent velocity V_t was derived considering that the iron abundance $\log A(\text{Fe})$ obtained from the given Fe I line is not correlated with the EW of that line.

The adopted value of the metallicity [Fe/H] was calculated using the iron abundance obtained from the Fe I lines. As is known, the lines of neutral iron are influenced by deviations from the local thermodynamic equilibrium (LTE), and therefore, that affects the iron abundances, which are determined from those lines. However, in the temperature and metallicity ranges of our target stars, the NLTE corrections do not exceed 0.1 dex (Mashonkina et al. 2011).

The comparison of the determined atmospheric parameters to the results obtained by other authors is presented in our previous studies (Mishenina et al. 2004, 2008). To additionally check our T_{eff} determinations, we compared the values T_{eff} with those for the recent IRFM observations by Casagrande et al. (2010). The mean difference $\langle \Delta(T_{\text{eff}} - T_{\text{eff}}^{\text{Cas}}) \rangle = -6 \pm 80$ K. The difference $\langle \Delta(T_{\text{eff}} - T_{\text{eff}}^{\text{Cas}}) \rangle$ as a function of T_{eff} and [Fe/H] is shown in Fig. 1. For most stars in our study, we used the values $\log g_{IE}$, determined by the iron ionization balance. The dependencies of $\log g_{IE} - \log g_P$ vs. T_{eff} and [Fe/H] are presented in Fig. 2. In both Figs. 1 and 2 there are no systematic differences. The average differences $\langle (\log g_{IE} - \log g_P) \rangle = -0.03 \pm 0.17$ for our target stars with $T_{\text{eff}} > 4800$ K.

In this paper, we also compare our data with the results of studies performed during recent years (Bensby et al. 2005; Reddy et al. 2006; Mashonkina et al. 2001; Peloso et al. 2005), in which the n-capture element abundances were also determined (see Table 1). As is evident from Table 1, the external accuracy of the effective temperature T_{eff} is within $\Delta T_{\text{eff}} = \pm 100$ K, the surface gravity $\log g - \Delta \log g = \pm 0.2$ dex.

4. Determination of the chemical composition

The abundances of the investigated elements Y, Zr, Ba, La, Ce, Nd, Sm, and Eu are determined for 276 F-G-K dwarfs under LTE approximation using the atmosphere models by Kurucz (1993).

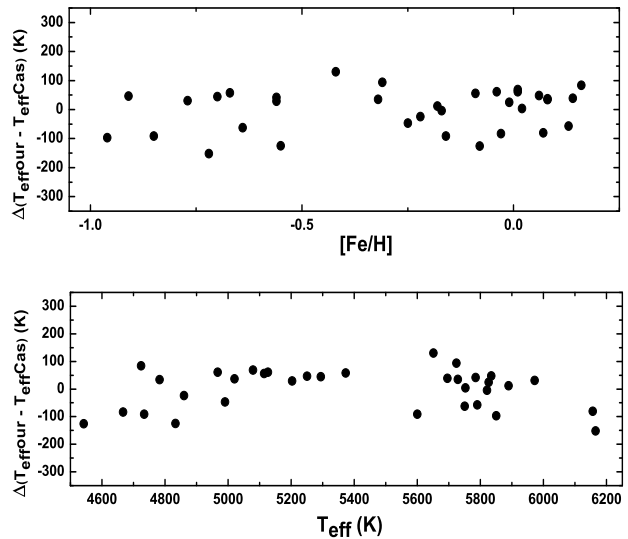


Fig. 1. Difference between the effective temperatures obtained in this work and those reported in Casagrande et al. (2010) for 33 stars in common (ΔT_{eff} vs. T_{eff} and ΔT_{eff} vs. [Fe/H])

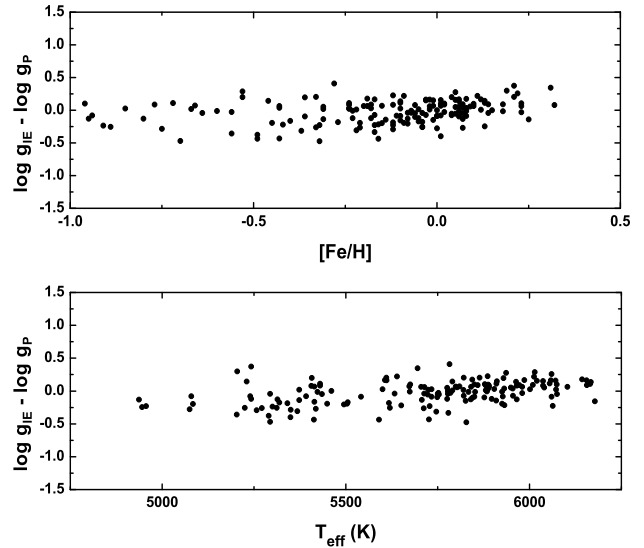


Fig. 2. Dependence of $\log g_{IE} - \log g_P$ upon T_{eff} and [Fe/H] for our sample stars.

The choice of model for each star was made by means of standard interpolation for T_{eff} and $\log g$. The determination of the Y, Zr, La, Ce, Nd, and Sm abundances was carried out using the EWs and code WIDH9 of Kurucz .

The Eu abundance was determined using a new version of the STARSP synthetic spectrum code (Tsymbal 1996), with the lines of Eu II 6645 Å and taking the hyperfine structure into account (Mashonkina 2000). The spectrum synthesis fitting of the Eu and Ba lines to the observed profiles are shown in Figs. 3,4. The abundance of the investigated elements were determined by differential analysis relative to the Sun. Solar abundances of Y, Zr, La, Ce, Nd, and Sm were calculated with the solar EWs, measured in the Moon and asteroids spectra, also obtained with the ELODIE spectrograph, and with the oscillator strengths $\log gf$ from Kovtyukh & Andrievsky (1999). The La and Sm lines are so weak that it is possible to neglect the hyperfine splitting

Table 1. Comparison of our parameters and abundance determinations with the results of other authors.

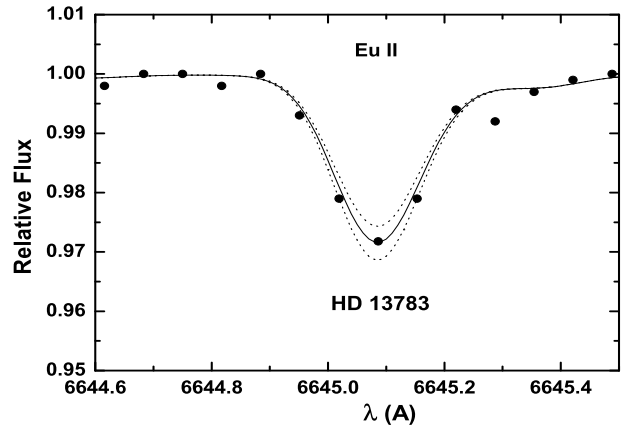
(Δ)	T _{eff}	log g	[Fe/H]	[Y/Fe]	n	[Zr/Fe]	n	[Ce/Fe]	n	[Nd/Fe]	n	[Sm/Fe]	n	[Eu/Fe]	n
Bensby et al. 2005	19 ±76	-0.09 ±0.19	-0.03 ±0.08	0.02 ±0.10	9									0.01 ±0.09	7
Reddy et al. 2006	92 ±29	-0.20 ±0.24	-0.01 ±0.04	-0.06 ±0.12	8			-0.09 ±0.09	7	-0.11 ±0.12				0.04 ±0.11	7
Mashonkina et al. 2001	19 ±64	-0.08 ±0.22	0.02 ±0.07	-0.10 ±0.07	16	-0.02 ±0.10	11	-0.11 ±0.07	15	-0.08 ±0.07	15			0.00 ±0.10	13
Peloso et al. 2005	46 ±66	-0.02 ±0.11	-0.02 ±0.06		5			0.01 ±0.06	5	-0.11 ±0.13	5	0.08 ±0.21	5		

Table 2. Parameters of the neutron-capture elements lines and the solar equivalent widths .

λ(Å)	Element	log gf	E _{low}	EW (mÅ)
4883.68	Y II	0.02	1.08	60
4900.11	Y II	-0.13	1.03	55
4982.13	Y II	-1.26	1.03	15
5087.42	Y II	-0.26	1.08	50
5119.11	Y II	-1.29	0.99	15
5200.41	Y II	-0.63	0.99	39
5289.82	Y II	-1.83	1.03	4.7
5402.77	Y II	-0.55	1.84	14
5728.89	Y II	-1.16	1.84	4.5
5112.28	Zr II	-0.85	1.66	8.4
5350.09	Zr II	-0.89	1.76	6.5
5350.36	Zr II	-0.80	1.81	6.5
4662.51	La II	-1.24	0.00	8.4
4748.74	La II	-0.54	0.92	5.7
5123.01	La II	-0.85	0.32	10.5
6320.41	La II	-1.33	0.17	6
4479.38	Ce II	0.42	0.56	24
4486.91	Ce II	-0.12	0.29	16.5
4560.28	Ce II	0.47	0.90	16
4562.37	Ce II	0.28	0.47	23
4773.96	Ce II	0.30	0.92	11
5274.24	Ce II	0.31	1.04	10.5
5610.25	Ce II	0.12	1.05	7
4462.92	Nd II	0.00	0.55	19
4811.35	Nd II	-0.89	0.06	9.6
4989.95	Nd II	-0.36	0.63	8.5
5089.83	Nd II	-1.09	0.20	4.8
5092.80	Nd II	-0.66	0.38	8
5130.60	Nd II	0.58	1.30	15.8
5234.21	Nd II	-0.38	0.55	10.5
5293.17	Nd II	-0.10	0.82	10.7
5319.82	Nd II	-0.34	0.55	11.5
4467.34	Sm II	0.19	0.65	13.5
4577.69	Sm II	-0.61	0.25	5.7
4791.60	Sm II	-0.97	0.10	4
4815.82	Sm II	-0.89	0.18	4.8

(HFS). The data for the neutron-capture element lines (including the solar EW) are given in Table 2.

The solar Eu abundance was also found by STARSP (Tsymbal 1996) via the line of Eu II in the Moon and asteroid spectra. The obtained solar abundances are the following: log A(Y) = 2.24, log A(Zr) = 2.60, log A(La) = 1.22, log A(Ce) = 1.55, log A(Nd) = 1.50, log A(Sm) = 1.01, log A(Eu) = 0.51, where log A(H) = 12. The differential approach for determining the relative abundance of the element A to the abundance of iron

**Fig. 3.** The spectrum synthesis fitting of the Eu line to the observed profiles. The change in Eu abundance is 0.05 dex.

relative to the solar ratio [A/Fe] was applied to reduce the influence of the spectrograph characteristics, and the errors are due to the uncertainties in the oscillator strengths and the deviations from the LTE upon the abundance definition.

For the barium abundance determination we used four lines of Ba II (4554, 5853, 6141, and 6496 Å) under the NLTE approximation. The NLTE profiles of the barium lines were computed using a modified version of the MULTI code (Carlsson 1986). The modifications are described in Korotin et al. (1999). Our barium model contains 31 levels of Ba I, 101 levels of Ba II with n < 50, and the ground level of the Ba III ion. In the analysis we included 91 bound-bound transitions.

The odd barium isotopes have hyperfine splitting of their levels and thus several HFS components for each line (Rutten 1978). Therefore, lines 4554 Å and 6496 Å were fitted by adopting the even-to-odd abundance ratio of 82:18 (Cameron 1982). The HFS for lines 5853 Å and 6141 Å is not significant.

Some uncertainty of the NLTE analysis of the barium spectrum is caused by the lack of information on the photoionization cross-sections for different levels. We used the results of the scaled Thomas-Fermi method application (Hofsaess 1979).

The effective collision strengths of electron excitation for the transitions between the first levels ($6s^2S$, $5d^2D$ and $6p^2P^0$) were used as in Schoening & Butler (1998). The experimental cross-sections for the transitions $6s^2S - 7s^2S$ and $6s^2S - 6d^2D$ were taken from Crandall et al. (1974). The collisional rates for the transitions between sublevels $5d^2D$, $6p^2P^0$ and $7s^2S$, $6d^2D$, as well as between $7s^2S$ and $6d^2D$, were estimated with the help of the corresponding formula by Sobelman et al. (1981). For

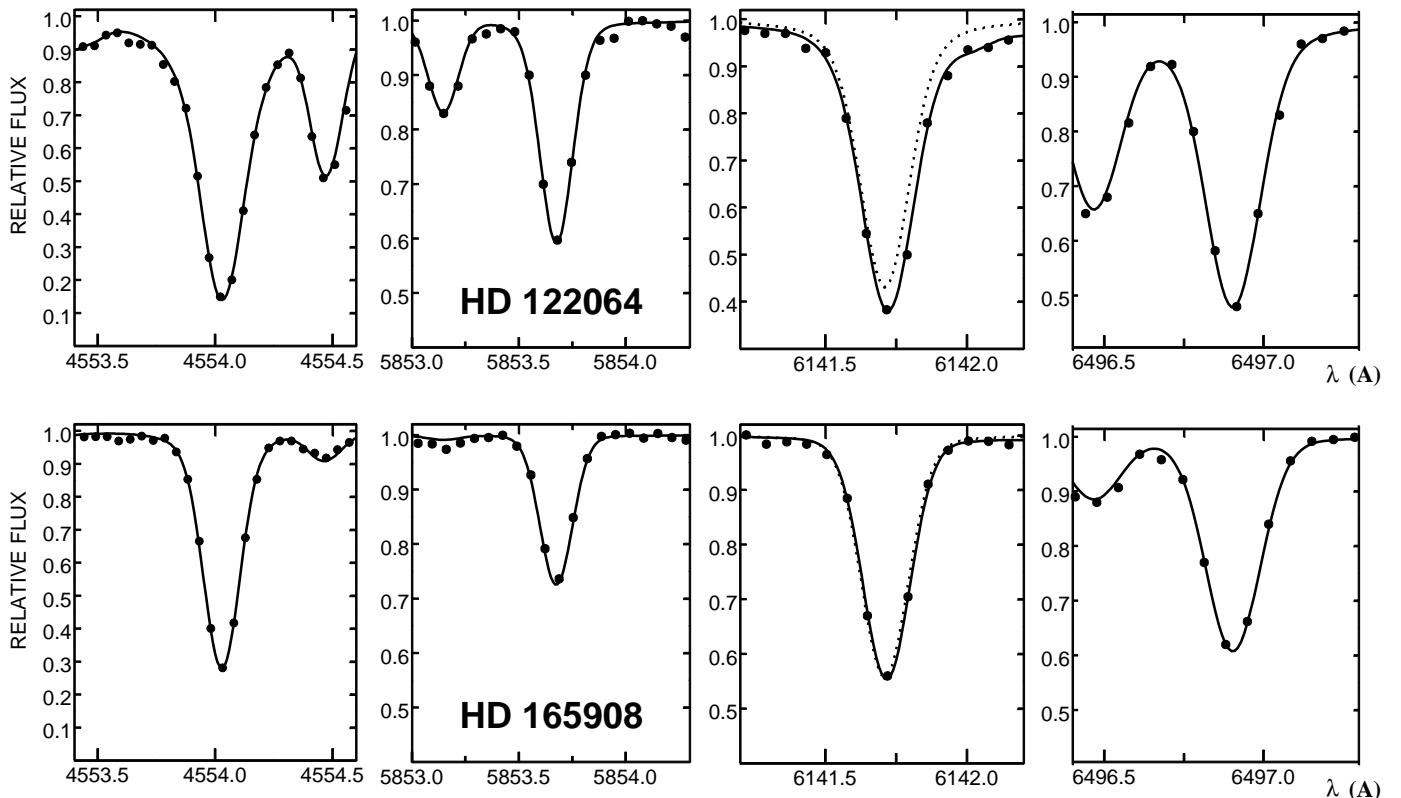


Fig. 4. Spectrum synthesis fitting of observed profiles of Ba lines. Line 6141 Å is blended with the iron line (the dotted line is the barium line profile). Computations are presented for the same barium abundance for four lines in each star.

the rest of the allowed transitions, we used the van Regemorter (1962) formula while the Allen (1973) formula was used for the forbidden transitions. The collisional ionization rate of the ground level of Ba II was computed with the appropriate formula from Sobelman et al. (1981). The more detailed description of the atomic model is given by Andrievsky et al. (2009) and Korotin et al. (2011). The adopted solar abundance of barium is equal to 2.17. The NLTE Ba abundances for 174 stars have been determined earlier by Korotin et al. (2011), for the other stars, the NLTE barium abundances are determined for the first time in the present paper.

The values of the Mg, Si, and Ni abundance were taken from our studies (Mishenina et al. 2004; Mishenina et al. 2008). The Mg abundances were computed under the NLTE approximation. For the stars that were investigated in Mishenina et al. (2004), the O and Ca abundances are determined in the present work, and the O, Ca values for the other stars were taken from the paper by (Mishenina et al. 2008). The O abundance was determined with a new version of the STARSP LTE spectral synthesis code (Tsymbal 1996). In this work we used the same line list as in Mishenina et al. (2008) in the region of the [O I] line 6300.3 Å.

5. Error analysis

The total errors in abundances result mainly from the errors in the choice of the parameters of the model atmospheres and in the EW measurements (the Gaussian fitting, placement of the continuum) in the case of Y, Zr, La, Ce, Nd, and Sm or in the fitting of the synthetic spectrum in the case of Eu and Ba. Table 3 lists the errors obtained when changing the atmospheric parameters by $\Delta T_{\text{eff}} = -100$ K (column 1); $\Delta \log g = +0.2$ (column

2); $\Delta V_t = +0.2$ km/s (column 3); and by assuming uncertainty of ± 2 mÅ in the EW and 0.03 dex in the calculated spectrum fitting. Those values were adopted taking the intrinsic accuracy into account for the atmospheric parameter determination, the processing of the spectra, and the comparison of our parameter definition with those of other authors. Those computations were performed for two stars with different characteristics, and the total error is given in column 4.

As seen in Table 3, the total uncertainty reaches 0.14 - 0.15 dex in the abundance determination for the stars with low temperatures, and its values are 0.08 - 0.13 dex for the hotter stars. The standard deviation, obtained by comparing our [Fe/H] determinations to those from other authors (Table 1), shows that we are consistent with them at the level lower than 0.11 dex.

6. Results and discussion

To discuss our results better, we report in Fig. 5 available measurements for the α -elements Mg and Si of the stars in the present stellar sample (Mishenina et al. 2004; Mishenina et al. 2008). The iron-group element Ni is shown in Fig. 6; heavy elements Y and Zr (elements representative of the neutron magic peak $N = 50$) in Fig. 7; Ba, La, Eu (s -process elements representative of the neutron magic peak $N = 82$, and Eu indicative of the r -process contribution) and Ce, Nd, Sm (also representative of the neutron magic peak $N = 82$) in Figs. 8 and 9, respectively. The complete elemental abundance data are given in Tables 4 and 5. The stars are marked according to their classification (see §2): full circles indicate the thick disk stars, open circles the thin disk stars, asterisks the Hercules stream stars and small circles are unclassified stars.

Table 3. Influence of stellar parameters on n-capture element abundance determination.

HD3765 ($T_{eff}=5079$, $\log g=4.3$, $[Fe/H]=0.01$) Total error				
	1	2	3	
Y	0	-0.11	0.04	0.12
Zr	-0.01	-0.14	0.01	0.14
Ba	0.02	-0.04	-0.07	0.10
La	-0.01	-0.15	-0.01	0.15
Ce	0.01	-0.10	0.02	0.10
Nd	0.03	-0.13	0.02	0.14
Sm	0.03	-0.13	-0.01	0.14
Eu	0.01	-0.09	-0.01	0.10

HD165401 ($T_{eff}=5877$, $\log g=4.3$, $[Fe/H]=-0.36$)				
	1	2	3	
Y	0.02	-0.07	0.02	0.08
Zr	0.02	-0.08	0.01	0.08
Ba	0.06	-0.03	-0.06	0.09
La	0.03	-0.12	0.00	0.13
Ce	0.03	-0.07	0.01	0.08
Nd	0.04	-0.08	0.01	0.09
Sm	0.04	-0.09	0.00	0.10
Eu	-0.01	-0.08	0.00	0.08

As for instance in Bensby et al. (2005), Reddy et al. (2006), Nissen & Shuster (2008), and Feltzing et al. (2009), our stellar sample also includes the thick disk stars at the solar metallicity and a metal-poor tail of the thin disk stars down to $[Fe/H] \sim -0.80$, allowing the analysis of different stellar populations across a wide range of metallicity.

6.1. The α -elements Mg and Si

In general, for Mg and Si in Fig. 5 (but see also heavier elements in Figs. 6, 7, and 8, and other α -elements), the stars of the thick disk show narrower dispersion than those of the thin disk. That could suggest that thick disk stars are formed from a more homogeneous material. The small number of the thick disk stars in our sample does not allow us to shed more light on that point of view. We refer to §6.3 for a detailed discussion about the nature of the thick and thin disk.

From Fig. 5, at the solar metallicity, the stars of the thin and thick disks tend to have similar chemical signatures. Then, with decreasing metallicity, all α -element signatures increase, confirming previous results by e.g., Bensby et al. (2003), Soubiran & Girard (2005), Mishenina et al. (2004), Reddy et al. (2006).

That trend of $[\alpha/Fe]$ versus metallicity can be understood well once the stellar nucleosynthesis feed-back to the galactic chemical evolution is considered. Indeed, below metallicity $[Fe/H] \lesssim -1$ the only relevant astrophysical source contributing to the chemical evolution of the α -elements and iron are core collapse Supernovae (CC-SN, see for instance Timmes et al. (1995) for the GCE calculations). Therefore, the roughly constant ratio O-Mg-Si-Ca/Fe observed for instance, in the halo stars (however, see the possible increase in $[O/Fe]$ at low metallicity, e.g., Mishenina et al. 2000) reflects a mixed contribution from CC-SN of different masses and (low) metallicities. On the other hand, for $[Fe/H] \gtrsim -1$, thermonuclear SN (SNIa, Hillebrandt et al. 2000) from remnants of low- and intermediate- mass stars has time to contribute to the chemical enrichment of the disk (see e.g., Matteucci et al. 2006), mostly feeding the iron-group elements and the α -elements, except for oxygen and magnesium (Thielemann et al. 1986; Travaglio et al. 2011; Kusakabe et al.

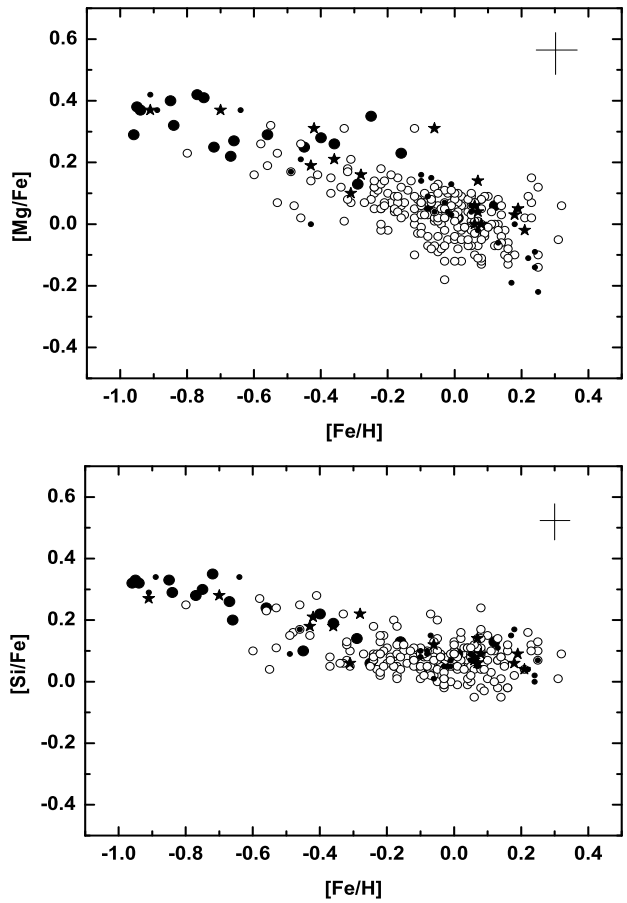


Fig. 5. Dependences of $[Mg/Fe]$ and $[Si/Fe]$ on $[Fe/H]$ for the stars of the thick disk (filled symbol), of the thin disk (open circle), the Hercules stream (asterisk), and unclassified stars (small circle).

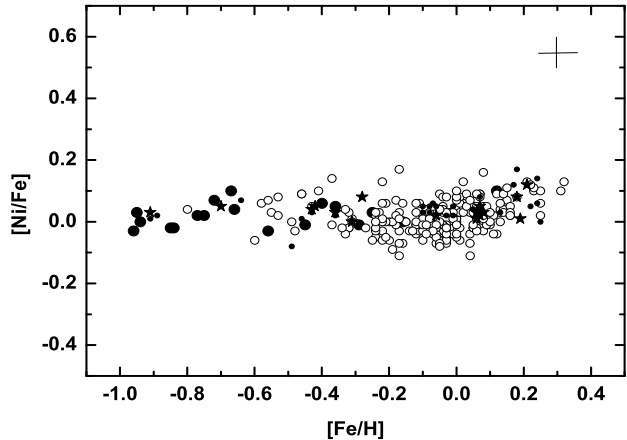


Fig. 6. Dependences of $[Ni/Fe]$ on $[Fe/H]$, the notation is the same as in Fig.5

2011). Therefore, the slope of the $[\alpha/Fe]$ ratio and the amount of departure from the solar ratio toward lower metallicities reflect the differential contribution from the CC-SN and SNIa to Fe and to the α -elements.

The $[Mg/Fe]$ observations in the thick disk stars show higher values than in the thin disk stars, as well as in the metallicity range where the two disks overlap ($-0.50 < Fe/H < 0$). The

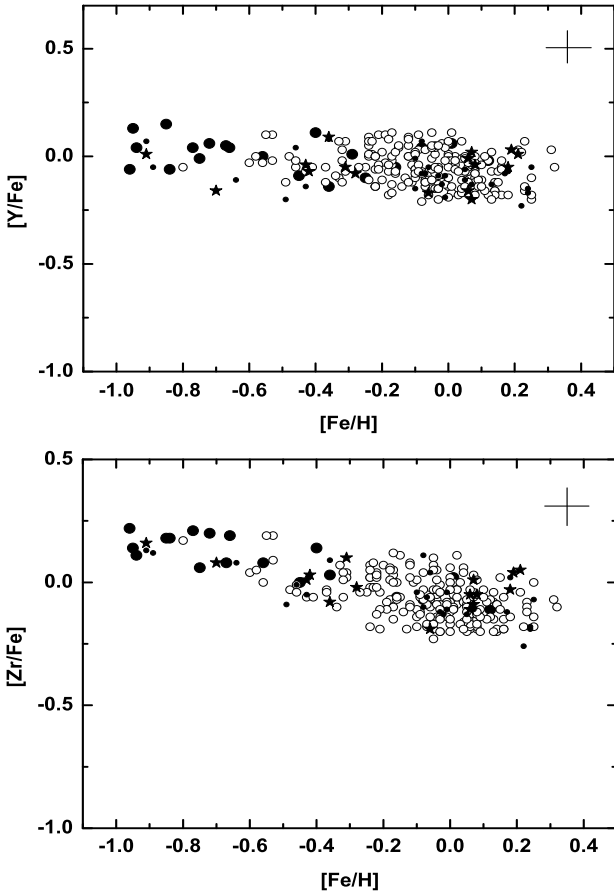


Fig. 7. Dependences of $[Y/Fe]$ and $[Zr/Fe]$ on $[Fe/H]$, the notation is the same as in Fig.5.

small number of the Mg measurements for the thick disk stars in our sample is not statistically significant, but does agree with previous, more extended studies. The ratio $[Mg/Fe]$ for the stars of the Hercules stream spans all values of both disks.

Several studies (Bensby et al. 2003; Fuhrmann 2004; Mishenina et al. 2004; Soubiran & Girard 2005; Reddy et al. 2006; and Bensby et al. 2007) have shown a magnesium abundance behavior with a “break” of the correlation between $[Mg/Fe]$ and $[Fe/H]$ at $[Fe/H] \sim -0.3$. Indeed, above $[Fe/H] \sim -0.3$, all stars with the thick disk kinematics show the Mg chemical signature typical of the thin disk. Reddy et al. (2006) also identify a small sample of thick disk stars with the thin disk abundance signature and $[Fe/H] \lesssim -0.3$, and defined all stars with thin disk $[Mg/Fe]$ and thick disk kinematics as the TKTA stars, belonging to an independent subgroup. Therefore, in this scenario, the metallicity of the thick disk would not exceed $[Fe/H] \sim -0.3$. On the other hand, other works (e.g., Mishenina et al. 2004) did not use such a distinction, simply assuming the existence of a “knee” in the $[Mg/Fe]$ trend toward $[Fe/H] \sim -0.2$ in the thick disk, making the thick overlap and thin disks abundance signature. Owing to the small number of the thick disk stars in the present sample, we cannot shed more light on this matter, even if we could define the TKTA stars or definitively defining them as the thick disk objects. Therefore, in this work, we consider them as the thick disk members, according to their kinematics alone. Standard thick disk stars show a dominant CCSN signature, whereas the TKTA-like stars are affected by a larger contribution from the SNIa, feeding Fe efficiently but not Mg.

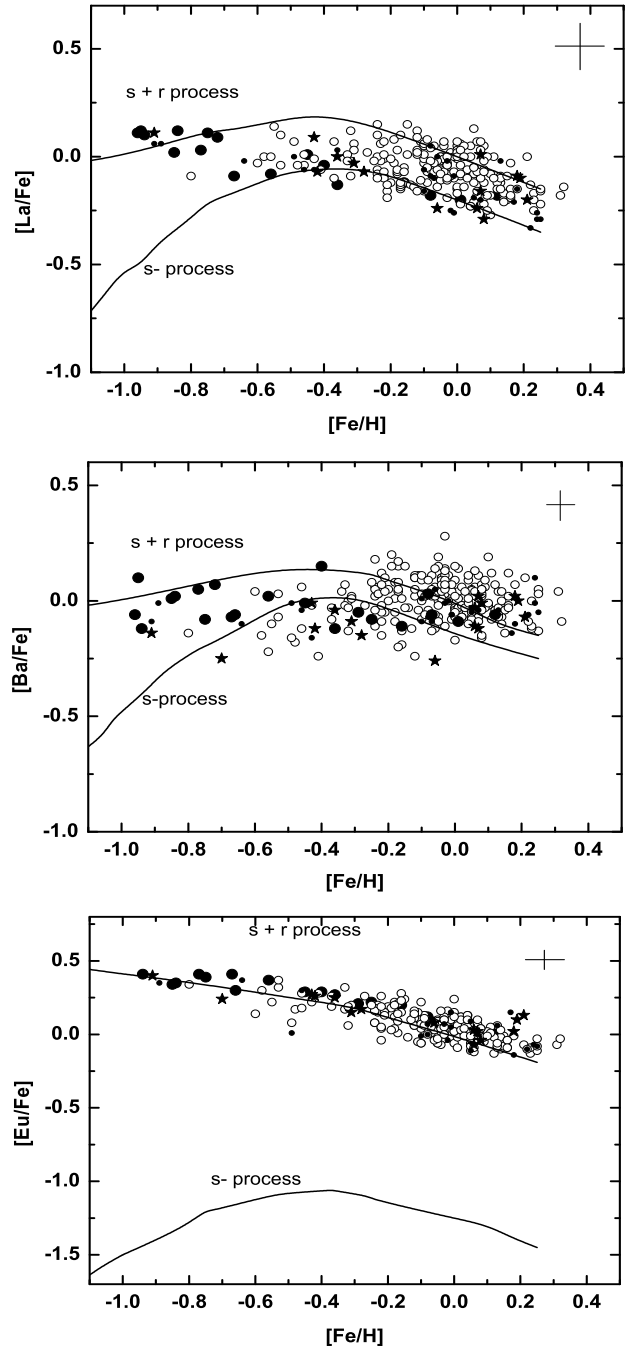


Fig. 8. Dependences of $[La/Fe]$, $[Ba/Fe]$, $[Eu/Fe]$ on $[Fe/H]$, the notation is the same as in Fig.5. The model calculations by Serminato et al. (2009) for the thin disk are marked with a solid line.

Therefore, they could have an abundance signature similar to the thin disk, not because they share some peculiar history compared to the rest of the thick disk objects, but simply because their pristine signature is more affected by SNIa. According to this picture, the TKTA stars should also have $[O/Fe]$ typical of the thin disk, since as mentioned oxygen is also not made in large amounts in SNIa. Furthermore, most of the TKTA stars in the Reddy et al. (2006) sample should be younger than standard thick disk stars with the same metallicity more likely carrying a stronger SNIa signature than do older objects. More TKTA-like stars need to be identified to draw a definitive picture.

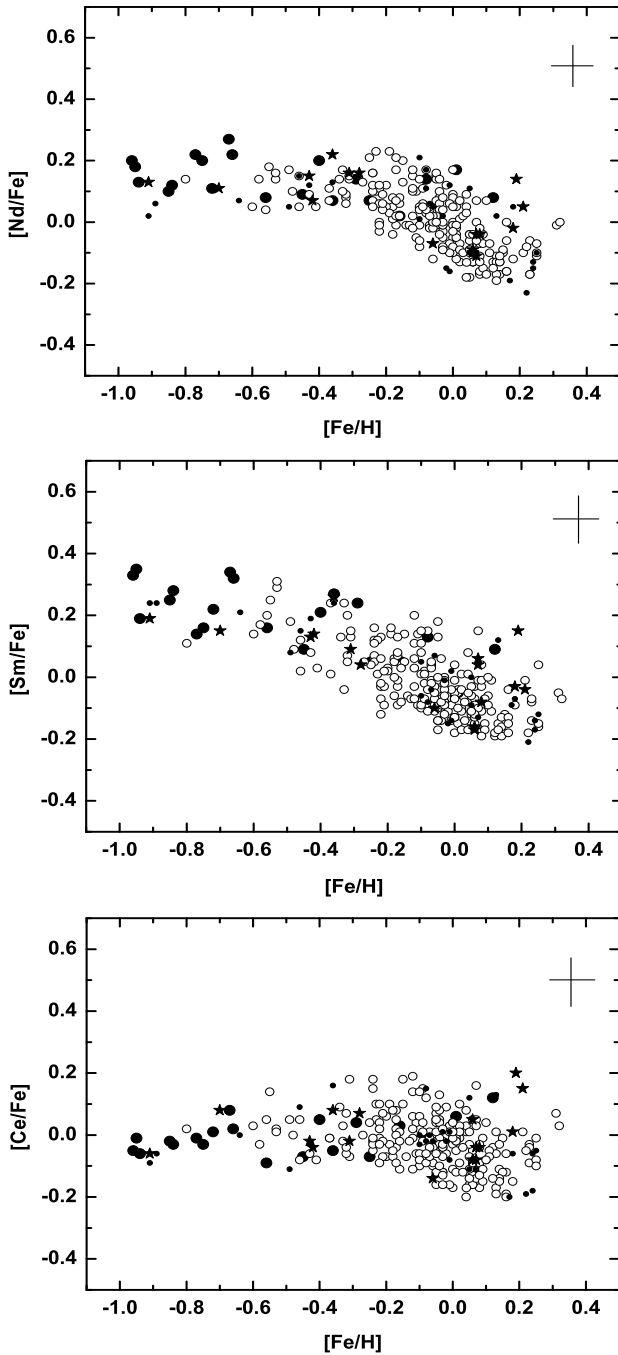


Fig. 9. Dependences of [Nd/Fe], [Sm/Fe], and [Ce/Fe] on [Fe/H], where the notation is the same as in Fig. 5

[Si/Fe] versus [Fe/H] shows behavior similar to that of [Mg/Fe], but with a smaller slope and with narrower dispersion. As we also have mentioned before, this is because the SNIa contribute more efficiently to the chemical evolution of the α -elements heavier than O and Mg, smoothing the effect of the strong iron production from those objects.

6.2. The iron-group element Ni

In Fig. 6, we show [Ni/Fe] versus [Fe/H], which is flat and roughly solar for the whole metallicity range, for the thin disk, the thick disk, and the Hercules stream stars. A slightly increasing trend may be possible for [Ni/Fe], for metallicity $[\text{Fe}/\text{H}] \geq$

0.1. The increasing trend of [Ni/Fe] toward higher metallicities than the solar ones is confirmed by other works, e.g. Neves et al. 2009. This is because Ni/Fe in the SNIa ejecta depends on the metallicity of the progenitor (e.g., Timmes et al. 2003, Bravo et al. 2010, Travaglio et al. 2005). In particular, the ejecta of unstable ^{56}Ni form the bulk of the produced iron. Its production tends to decrease with the increasing metallicity, whereas most of Ni is produced in the NSE conditions, and its production is quite constant with metallicity. Therefore, the consequent [Ni/Fe] is expected to increase in the disk with [Fe/H]. A flat trend for [Ni/Fe] at solar metallicity may be explained if the average Ni/Fe ratio in the CCSN ejecta is similar to the SNIa signature. No significant slope or dispersion is observed in that case. The Ni/Fe ratio in SNIa ejecta may change quite significantly from different theoretical predictions, from a ratio that is two to three times higher than the solar one (e.g., Thielemann et al. 1986; Travaglio et al. 2011) to a ratio close to the solar one (e.g. Thielemann et al. 2004). Present observations seem to support those predictions more.

6.3. AMR for the thick and thin disks

In the previous sections, we discussed the abundance signature of the α -elements and Ni. All those elements that include Fe are primary. Their yields from the CCSN or SNIa do not depend significantly on the initial metallicity of the parent star. As mentioned above, the abundance dispersion (besides observational errors) and the [El/Fe] slope are given by the differential contribution (i.e., by the different elemental ratio in the ejecta) between the CCSN and SNIa.

This is not the case for the *s*-process. Therefore, before discussing observations for heavy elements, we revise the age-metallicity relation in the thick and thin disks in this section. As is well known, the age-metallicity relation for the thick disk stars show a signature of decreasing age with increasing metallicity, with some dispersion (e.g., Bensby et al. 2007).

On the other hand, the stars belonging to the thin disk tend to show wide metallicity dispersion, in particular around the time of formation of the Sun, and there is no clear trend in age versus metallicity. Indeed, as written in Bensby et al. (2007), “the most metal-rich thin-disk stars evidently are not the youngest ones”. A possible proposed scenario to explain that missing trend is an infall of fresh material in the thin disk around the time of the Sun’s formation, causing a spread in metallicity for the stars of the same age and, more in general, a dilution of metals available in the interstellar medium at that time produced by previous stellar generations (Edvardsson et al. 1993; Feltzing et al. 2001; Haywood 2006).

Such a contribution could have had a small impact in the [El/Fe] ratio in the disk at that stage, but the average [El/H] abundance was probably modified (and possibly reduced) by the dilution with fresh material, including the [Fe/H]. Furthermore, the yields of nucleosynthesis processes that are affected by the initial metallicity of the star (secondary) will be affected by such a dispersion. For instance, the *s*-process yields from the AGB stars or massive stars, born in the thin disk about 5 Gyr ago, will carry the signature of nonuniform pristine metal content, affecting the abundance signature in the youngest generations of evolving and unevolved stars.

In Fig. 10 we show the age versus metallicity relation for the thin disk stars in our sample as derived from different analyses based on two sets of stellar tracks, by Mowlavi et al. (2012) and Holmberg et al. (2009). In the first case, to estimate the age we use the python k-d tree based interpolation technique. Keeping

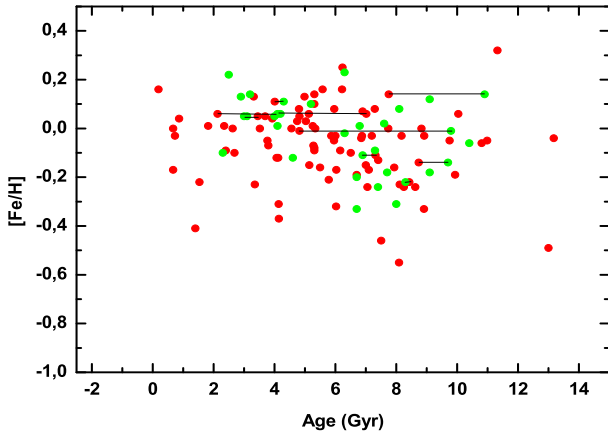


Fig. 10. Dependence of $[Fe/H]$ on age for the thin disk stars in our sample according to Holmberg et al. (2009) (green points) and Mowlavi et al. (2012) (red points). Common stars in the two samples are connected by a continuous line.

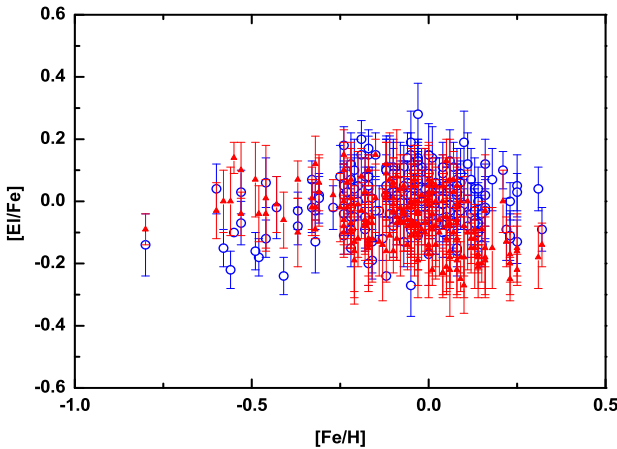


Fig. 11. The $[Ba/Fe]$ and $[La/Fe]$ trends with $[Fe/H]$ and error determination bars for each star (open blue circles and red triangles, respectively).

into account the observed metallicity for each star, in the figure we include only the objects fitted by the correct isochrones set with pairwise euclidean distances in two-dimensional space (given by T_{eff}/T_{\odot} and L/L_{\odot}) smaller than 0.02.

In the second case (Holmberg et al. 2009¹), ages are based on the theoretical isochrones from Padova (Girardi et al. 2000) and the photometric metallicities used. We include only stars with reported errors in the age estimation smaller than 25%. The spread of predictions using different set of isochrones is mainly due to the stellar uncertainties. In the figure ten stars are fitted by both Holmberg et al. (2009) and Mowlavi et al. (2012) within the mentioned criteria. For six of them the age estimation is consistent within 2 Gyr, whereas for the remaining stars there is larger discrepancy (namely, HD 28447, HD 70923, HD 178428, and HD 75767).

According to the results obtained for our sample thin disk stars with different stellar track compilations, we confirm wide dispersion of the age-metallicity relation, in particular at the time of the Sun's formation (e.g., Bensby et al. 2007). Using the tracks from Holmberg et al. (2009) and Mowlavi et al. (2012),

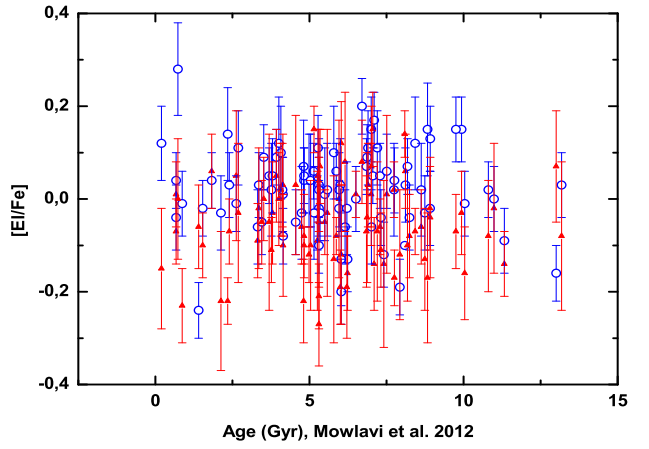


Fig. 12. $[Ba/Fe]$ and $[La/Fe]$ trends versus age determined by us according to Mowlavi et al. (2012) (top panel) and according to Holmberg et al. (2009) (bottom panel). The notation is the same as in Fig. 11.

the metallicity dispersion does not decrease for younger stars, and such a trend is not observed. Therefore, within the present uncertainties, a specific trend for the age versus metallicity cannot be observed (in agreement with Bensby et al. 2007), as is instead possible for the thick disk stars. We do not consider here the thick disk stars since our sample is too small to derive any specific conclusion, although we may confirm the age-metallicity trend for the thick disk (Soubiran & Girard 2005). Such a result for local metallicity dispersion and AMR is also confirmed by recent reanalysis of the metallicity distribution function of the solar neighborhood over the Geneva-Copenhagen survey (Casagrande et al. 2011). Forthcoming results from the RAVE survey (Steinmetz et al. 2006) will probably improve present scenario and shed more light on the age-metallicity dispersion and its trend for the thin disk stars.

In several previous works (Haywood 2006, etc), the uncertainty related to the age definition by fitting stellar luminosity and surface temperature has been largely discussed. Stellar model uncertainties are affecting theoretical calculations within isochrones sets. Different choices for macrophysics (e.g., convection criteria and mass loss) and microphysics (e.g., opacities, equation of state, nuclear physics reaction rates) may introduce significant discrepancies between different stellar theoretical predictions. However, despite offsets from one isochrone set to the other and large uncertainties of 2 Gyr or more for several

¹ <http://cdsarc.u-strasbg.fr/viz-bin/Cat?V/130>

stars, the different AMR behavior for the thin and thick disks is robust, compared to different sets of the stellar models.

6.4. Heavy neutron-capture elements

The Y and Zr elements belong to the neutron magic peak $N = 50$. Several processes are likely to be responsible for their nucleosynthesis in stars. During early stages of the chemical evolution of the Galaxy they can be made by the *r*-process (reproducing 8 and 15 per cent of their solar abundance, respectively, Travaglio et al. 2004). Another component active in the early Universe has been identified in several stars (e.g., Truran et al. 2002; Honda et al. 2006; Chiappini et al. 2011), unrelated to the main *r*-process. Several scenarios have been proposed, such as charged particle reactions in the SN explosive nucleosynthesis (e.g., Hoffman et al. 1996; Qian & Wasserburg 2008) and in neutrino winds (Frohlich et al. 2006; Farouqi et al. 2009; Arcones et al. 2011) or the *s*-process in fast rotating massive stars (Pignatari et al. 2008; Frischknecht et al. 2012). It is also a matter of debate whether the process(es) possibly responsible for the Sr-Y-Zr enrichment of those old stars is(are) active until the solar metallicities as a primary process. Indeed, Travaglio et al. (2004) identified a similar missing component in the solar system *s*-process distribution (lighter element primary process, or LEPP). In the latter case, the LEPP would be responsible for about 20% of solar Y and Zr. Finally, the rest of Y and Zr is made by the *s*-process mostly in the AGB stars with some minor contribution from massive stars. In both cases, their *s*-process production from the AGB stars becomes relevant quite late for the chemical evolution, reaching a contribution peak at about $[Fe/H] \sim -0.4$ with an approximately constant (for Y) or slight decrease (for Zr) for higher metallicities ($[Fe/H] \gtrsim -0.4$, Travaglio et al. 2004).

The light *s*-process elements Y and Zr show different trends in $[Fe/H]$. The $[Y/Fe]$ ratio versus $[Fe/H]$ shows a more or less flat trend in our stellar sample. Similar results are obtained by Reddy et al. (2006). Bensby et al. (2005) show a $[Y/Fe]$ that is lower by 0.1–0.15 dex for $[Fe/H] \lesssim -0.3$. The $[Zr/Fe]$ ratio versus $[Fe/H]$ increases by about 0.2 dex with decreasing metallicity. Indeed, within some dispersion of abundances in the thin disk stars, the average abundances of the thick disk stars $[Fe/H] \lesssim -0.3$ are on average larger than for stars at the solar metallicity. Such differences between Y and Zr could be because Y receives a larger *s*-process contribution than Zr in particular in the thin disk, compensating more efficiently for the iron made by SNIa. Indeed, the GCE calculations by Travaglio et al. (2004) can account at least qualitatively for such a variation, because of the higher *s*-process contribution to Y than to Zr (according to Travaglio et al. 2004, 74% and 67%, respectively), and because as we mentioned, the Zr *s*-process yields from the AGB stars start decreasing earlier than Sr and Y with increasing metallicity, as above $[Fe/H] \gtrsim -0.3$. (see e.g., Travaglio et al. 2004).

Barium and La are the *s*-process elements at the neutron magic peak $N=82$, with a smaller contribution from the *r*-process. The trend $[Ba/Fe]$ versus $[Fe/H]$ shows a significant dispersion and, on average, an underabundance of $\lesssim 0.2$ dex in the thick disk compared to the thin disk. The $[La/Fe]$ ratio tends to show a slightly decreasing trend to $[Fe/H] > 0$ for the thin disk and the Hercules stream stars, but with a large dispersion that is the same as for Ba. To compare the behavior of two *s*-process elements more easily, we show in Fig. 11 together the $[Ba/Fe]$ and $[La/Fe]$ versus $[Fe/H]$, including observational uncertainties, only for the thin disk stars. From the figure, both elements show a dispersion of about 0.4 dex, ranging between $-0.2 \lesssim [El/Fe] \lesssim +0.2$, as well as similar trends that are difficult to disentangle.

Europium is mainly formed by the *r*-process, showing a marked trend with $[Fe/H]$ and a slight overabundance for the thick disk stars. Since the bulk of Eu is created in massive stars, the $[Eu/Fe]$ ratio is expected to decrease once Fe from the SNIa starts to play a role in the chemical evolution of the disk. Therefore, the thick disk shows a higher $[Eu/Fe]$ on average, than does the thin disk. A similar general trend is observed for Nd and Sm, since both of them, like Eu, receive a major contribution from the *r*-process.

Finally, the Ce abundance seems to behave similarly in all substructures, and it shows a relevant dispersion that agrees with Reddy et al. (2006). A slightly decreasing trend could be seen for $[Fe/H] > -0.2$ in the thin disk, but it is not followed by all the stars. Therefore, the similar consideration as made for Ba and La still holds for Ce. In summary, compared to the thick disk, the thin disk stars are created by a more complex combination of contributions from massive stars, *r*-process, SNIa, and AGB stars.

On the other hand, typical disk stars with metallicity $[Fe/H] \gtrsim -1$ (i.e., once the iron contribution from the SNIa starts to be observed), may start carrying an evident signature of the *s*-process yields from the AGB stars, which are the parents of thermonuclear supernovae. That is clearly shown in Fig. 13, where $[Nd/Ba]$ and $[Nd/Eu]$ versus $[Fe/H]$ for stars in our sample are given in comparison with the $[Nd/Ba]_r$ and $[Nd/Eu]_r$ observed by Mashonkina et al. (2004). On average, the stars that are already in the thick disk show relatively low $[Nd/Ba]$ and $[Nd/Eu]$, which is higher than those observed for the pure *r*-process signature, as expected from the *s*-process contribution by the AGB stars with the thick disk metallicities.

In Fig. 8, we compare the observations for La, Ba and Eu with GCE calculations by Serminato et al. (2009). In particular, in the Serminato et al. (2009) simulations, the contribution from the *s*-process in low-mass AGB stars and from the *r*-process are included. For those elements, both neutron capture processes need to be considered in order to obtain the solar abundance. A small scatter is observed for Eu, consistent with the GCE predictions once both *r*-process and small *s*-process contributions are included. On the other hand, both $[La/Fe]$ and $[Ba/Fe]$ show large dispersion for the thick and thin disk stars, possibly increasing towards the solar and super-solar metallicities. No clear trend can be identified with such a dispersion, which by definition cannot be reproduced by the single-zone GCE calculations of Serminato et al. (2009). Also the GCE decreasing trend in $[Ba/Fe]$ and $[La/Fe]$ for $[Fe/H] > -0.3$ is not clearly identifiable, even if several stars fall along the Ba and La theoretical curves.

Compared to the α -elements, the *s*-process elements La and Ba show similar dispersion at high metallicities, but the GCE evolutionary trends are not clearly reproduced. The reason is that the α -elements (as well as Fe) are primary, and their chemical evolution is affected by the age and, only marginally, by the metallicity. Therefore, the use of decent stellar yields from core-collapse SNe and SNIa allows the chemical evolution trends of Fe and α -elements to be predicted with reasonable accuracy, once the weight of two main yield donors is known for the Sun. In our case, Fe provided a phenomenological indicator of such a weight, and it is not surprising that one-dimensional GCE models may reproduce the $[\alpha/Fe]$ trend of the thick and thin disks well.

On the other hand, Ba and La are mostly created by the *s*-process in the AGB stars, whose contribution to the interstellar medium depends on metallicity, as clearly shown by, e.g., Travaglio et al. (2004), and on the age: i.e., on the different life timescale of the stars with different initial mass. If the age

versus metallicity relation of a stellar system is linear (e.g., the thick disk in its lowest metallicity population), then the *s*-process abundances are expected to show a similar dependence on the age and metallicity, and therefore simple theoretical GCE calculations may provide a reasonable fitting of observations. As we discussed in the previous section, this is not the case for the thin disk, where a wide spread of metallicity is observed for the stars of the same age, and there is no clear age versus metallicity evolution trend. A wide abundance dispersion therefore observed, independently for the event that causes such a spread, and simple GCE models may lose their predictive power for the *s*-process elements. To consistently compare the stellar abundances with GCE predictions, a preliminary selection of stars with the same location in the thin disk and that fall on the same age - metallicity slope should be performed. Such a sample of stars would be representative of a specific subgroup. A comprehensive GCE study of the thin disk would be given by taking those different populations into account, and therefore, would require multidimensional GCE simulations (e.g., Minchev et al. 2012).

Similar conclusions may be obtained for Ce in Fig. 9, which is an *s*-process element as Ba and La. Sm receives a comparable contribution from the *s*- and *r*- processes, and as expected, the [Sm/Fe] ratio shows a clearer decreasing trend with increasing metallicity.

Summing up, the trend of [Eu/Fe] is reproduced well by the GCE simulations, since Eu is made mostly by the *r*-process (that is primary), and the chemical evolution models are well constrained in the Fe evolution. The [α /Fe] show some dispersion in the disk stars, due to the differential contribution from the core-collapse SNe and SNIa to the initial stellar abundances. Since their production in the primary, the GCE calculations can reproduce a general trend quite well, once the age of the stellar system together with basic evolution properties (e.g., IMF) are given. Finally, the *s*-process elements Ba, La, and Ce are not primary, and due to the lack of an age versus metallicity relation in the late disk their dispersion and evolutionary trends become more difficult to predict.

In Fig. 12 we show [Ba/Fe] and [La/Fe] for the stars in our sample with respect to the age estimated from stellar tracks by Mowlavi et al. (2012) and Girardi et al. (2012). With the abundance dispersion and uncertainties, we find it difficult for both references to clearly identify in our sample of stars any increase in [Ba/Fe] for youngest stars, as suggested by Bensby et al. (2007) for the thin disk, or by D’Orazi et al. (2009) and Maiorca et al. (2012) for open clusters (however, see D’Orazi et al. 2012 where possible observational issues are discussed for metal-rich open clusters). The same conclusion is obtained for [La/Fe]. The dispersion of [Ba/Fe] and [La/Fe] for the stars with the same age may be due to different chemical enrichment histories inside the thin disk.

7. Conclusions

We present and examine the abundance of the iron peak element Ni, and of the neutron-capture elements Y, Zr, Ba, La, Eu, Nd, Sm and Ce for 276 stars belonging to different substructures of the Galaxy, separated according to kinematic criteria. For most of the stars in this sample, the abundances of neutron-capture elements have not been measured before.

Concerning Ni, all stellar structures show a flat trend up to $[Fe/H] \sim 0.1$ with an [Ni/Fe] close to the solar one, with a slight increase for the super-solar metallicities. That implies that both CCSN and SNIa ejecta should have an Ni/Fe yield ratio close to the solar one and that the relative contribution to the Ni and

Fe inventory in the solar system from these two different astrophysical sites should be similar, with the SNIa producing about two-thirds of the solar Fe and Ni. For the stars with $[Fe/H]$ over ~ 0.1 , the observed increasing trend of [Ni/Fe] can be explained by the decrease in the Fe yields from the SNIa with the increasing metallicity.

Considering four different sets of theoretical stellar tracks, we showed that under large uncertainties it is not possible to define a clear age - metallicity trend in the thin disk stars from our sample, as already pointed out for the thin disk. That will not affect the chemical evolution of the primary elements such as the α elements and Ni too much, instead of that, we expect it to cause a noticeable dispersion for the elements whose production can change significantly with metallicity.

We discussed the differences between the Y and Zr trends. In particular, the [Zr/Fe] ratio is slightly higher in the thick disk compared to the thin disk (~ 0.2 dex). On the other hand, the [Y/Fe] shows a flat trend in first approximation for the observed metallicity range. Such a difference may be due to a larger primary contribution to Zr compared to Y, by the *r*-process and the LEPP component, as predicted by the theoretical calculations.

Ba, La, and Ce are mostly produced by the *s*-process in the AGB stars, with their yields significantly affected by the initial metal content in the range of the metallicity considered. In our stellar sample, the thin disk stars show a dispersion of about 0.4 dex at the solar-like metallicity. For $[Fe/H] \gtrsim 0.1$, they may start showing a decreasing trend, at least for the bulk of the stars, noticeable in particular for La. We cannot confirm any particular trend by [Ba/Fe] and [La/Fe] versus the age, also due to the large uncertainties in age determination.

Eu is mainly made by the primary *r*-process. We confirmed its decreasing trend with metallicity, which was also observed in previous works. In particular, in our stellar sample we found a really small dispersion, and it is well reproduced by the GCE calculations.

Finally, for the metallicities typical of the thick disk, [Sm/Fe] and [Nd/Fe] show a higher ratio than the solar one, due to the larger *r*-process contribution compared to Ba, La, and Ce (comparable to the *s*-process contribution for Nd, and around 70 % for Sm). Within uncertainties and intrinsic dispersion, most of the stars show a decreasing trend for Sm moving from the typical thick disk metallicities to the thin disk ones, such as for Eu. For Nd, we found a more similar trend to the *s*-process elements discussed before, with [Nd/Fe] decreasing with metallicity for $[Fe/H] \gtrsim 0$, and at the same time an increase in the abundance dispersion.

Acknowledgements. The authors thank the anonymous referee for a careful reading of the manuscript. TM thanks Prof. I.L. Andronov for some suggestions. This work was supported by the Swiss National Science Foundation (SCOPES project No. IZ73Z0-128180). MP thanks the Ambizione grant of the SNSF (Switzerland) for support. FKT, MP, and CC also thank to Eurogenesis. TM is grateful the Laboratoire d’Astrophysique de Bordeaux for their kind hospitality.

References

- Allen, C.W. 1973, Astrophysical Quantities (London: Athlone Press)
- Allende Prieto, C., Garcia Lopez, R.J., Lambert, D.L. & Gustafsson, B. 1999, ApJ, 527, 879
- Andrievsky, S. M., Spite, M., Korotin, S. A. et al. 2009, A&A, 494, 1083
- Arcones, A., & Montes, F. 2011, ApJ, 731, 5
- Baranne, A., Queloz, D., Mayor, M. et al. 1996, A&AS, 119, 373
- Bensby, T., Feldzins, S., & Lundstrom, I. 2003, A&A, 410, 527
- Bensby, T., Feltzing, S., Lundstrom, I., & Ilyin, I. 2005, A&A, 443, 185
- Bensby, T., Zenn, A.R., Oey, M.S., & Feltzing, S. 2007, A&A, 663, L13
- Bienaymé, O., Soubiran, C., Mishenina, T. et al. 2006, A&A, 446, 933

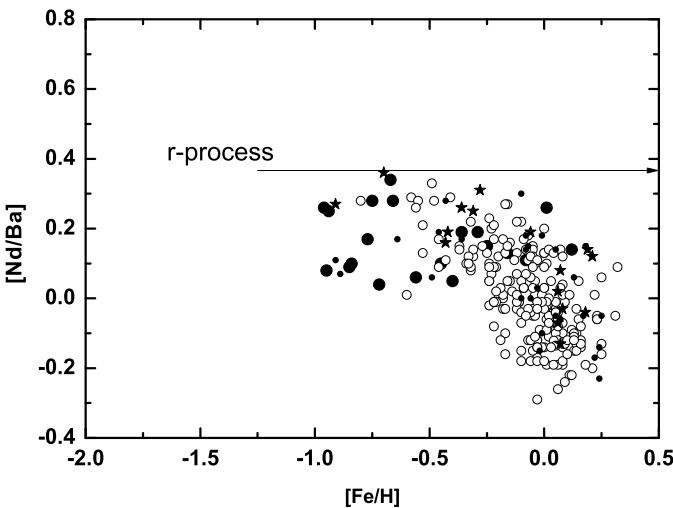


Fig. 13. Dependence of [Nd/Ba] on [Fe/H], the notation is the same as in Fig.5

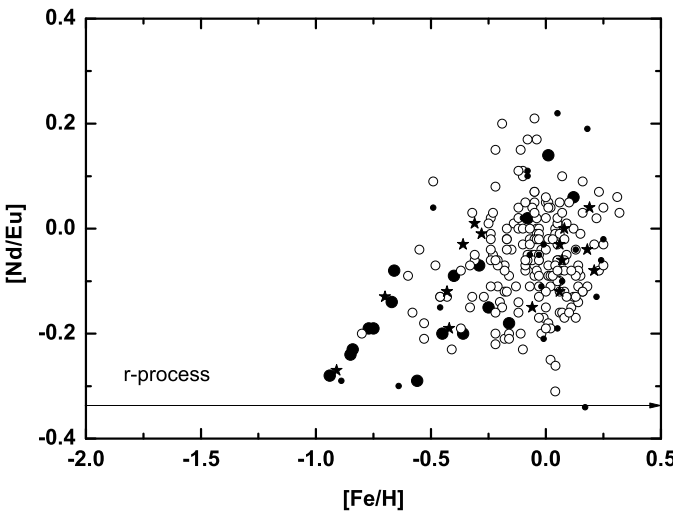


Fig. 14. Dependence of [Nd/Eu] on [Fe/H], the notation is the same as in Fig.5

- Bisterzo, S., Gallino, R., Straniero, O., Cristallo, S., & Käppeler, F. 2011, MNRAS, 418, 284
 Bravo, E., Dominguez, I., Badenes, C., Piersanti, L., & Straniero, O. 2010, ApJ, 711, 66
 Brewer, M.M., & Carney, B. 2006, A&A, 131, 431
 Burbidge, E. M., Burbidge, G. R., Fowler, W.A., & Hoyle, F. 1957, Reviews of Modern Physics, 29, 547
 Cameron, A. G. W. 1957, AJ, 62, 9
 Cameron, A.G.W. 1982, A&AS, 82, 123
 Carlsson, M. 1986, Uppsala Obs. Rep. 33
 Casagrande, L., Ramirez, I., Meléndez, J., Bessell, M., & Asplund, M. 2010, A&A, 512, 54
 Casagrande, L., Schonrich, R., Asplund, M., Cassisi, S., Ramirez, I. et al. 2011, A&A, 530, 138
 Chiappini, C., Frischknecht, U., Meynet, G. et al. 2011, Nature, 474, 666
 Crandall, D.H., Dunn, G.H., Gallagher, A. et al. 1974, ApJ191, 789
 da Silva, L., Girardi, L., Pasquini, L. et al. 2006, A&A, 458, 609
 D'Orazi, V., Magrini, L., Randich, S., et al. 2009, ApJ, 693, 31
 D'Orazi, V., Biazzo, K., Desidera, S., et al. 2012, MNRAS, 423, 2789
 Edvardsson, B., Andersen, J., Gustafsson, B., et al. 1993, A&A, 275, 101
 Eggen, O.J. 1958, MNRAS, 118, 154
 Famaey, B., Jorissen, A., Luri, X., et al. 2005, A&A, 430, 165
 Farouqi, K., Kratz, K.-L., Mashonkina, L. I., et al. 2009, ApJ, 694, 49
 Feltzing, S., Holmberg, J., & Hurley, J. R. 2001, A&A, 377, 911
 Feltzing, S., Oey, S., & Bensby, T. Proc.IAU Symp., 2009, 254, 197.
 Freiburghaus, C., Rosswog S., & Thielemann, F.-K. 1999, ApJ, 525, L121
 Frischknecht, U., Hirschi, R., & Thielemann, F.-K. 2012, A&A, 538, 2
 Fröhlich, C., Martinez-Pinedo, G., Liebendorfer, M., et al. 2006, Phys. Rev. Lett., 96, 142502
 Fuhrmann, K. 2004, Astronomische Nachrichten, 325, 3
 Fux, R. 2001, A&A, 373, 511
 Gallino, R., Arlandini, C., Busso, M., et al. 1998, ApJ, 497, 388
 Galazutdinov, G.A. 1992, Preprint SAO RAS, n92
 Gilmore, G. & Reid, N. 1983, MNRAS, 202, 1025
 Girardi, L.; Bressan, A., Bertelli, G., & Chiosi, C. 2000, A&AS, 141, 371
 Girardi online http://stev.oapd.inaf.it/~lgirardi/cgi-bin/param_1.0
 Haywood, M. 2006, MNRAS, 371, 1760
 Hillebrandt, W., Niemeyer, J. C., & Reinecke, M. 2000, ARA&A, 38, 191
 Hoffman, R. D., Woosley, S. E., Fuller, G. M., & Meyer, B. S. 1996, ApJ, 460, 478
 Hofsaess, D. 1979, ADNDT 24, 285
 Holmberg, J., Nordstrom, B., & Andersen, J. 2009, A&A, 501, 941
 Honda, S., Aoki, W., Ishimaru, Y., Wanajo, S., & Ryan, S.G. 2006, ApJ, 643, 1180
 Jorgensen, B. R. & Lindegren, L. 2005, A&A, 436, 127
 Käppeler, F., Beer, H., Wisshak, K. 1989, Reports on Progress in Physics, 52, 945
 Katz, D., Soubiran, C., Cayrel, R. et al. 1998, A&A, 338, 151
 Klochkova, V., Mishenina, T., Korotin, S., et al. 2011, Ap&SS, 335, 141
 Korobkin, O., Rosswog, S., Arcones, A., Winteler, C. 2012, MNRAS, 426, 1940
 Korotin, S.A., Andrievsky, S.M., & Luck, R.E. 1999, A&A351, 168
 Korotin, S., Mishenina, T., Gorbaneva, T., & Soubiran, C. 2011, MNRAS, 415, 2093
 Kovtyukh, V.V., Soubiran, C., & Belik, S.I. 2004, A&A, 427, 923
 Kurucz R.L. 1993, CD ROM n13
 Kusakabe, M., Iwamoto, N., & Nomoto, K. 2011, ApJ, 726, 25
 van Leeuwen F. 2007, ASSL, 350
 Maiorca, E., Randich, S., Busso, M., Magrini, L., & Palmerini, S.E. 2011, ApJ, 736, 120
 Marsakov, V.A., Borkova, T.V. 2005, Astronomy Letters, 31, 515
 Mashonkina, L., Gehren, T. 2000, A&A, 364, 249
 Mashonkina, L.I. 2000, Astr. Rep. 44, 558
 Mashonkina, L.I., Gehren, T. 2001, A&A, 376, 232
 Mashonkina, L.I., Kamaeva, L.A., Samtoev, V.A., & Sakhibullin, N.A. 2004, Astr. Rep., 48, 185
 Mashonkina, L.I., Gehren, T., Shi, J.-R., Korn, A.J., Grupp, F. 2011, A&A, 528, A87
 Matteucci, F., Panagia, N., Pipino, A., Mannucci, F., Recchi, S., Della Valle, M. 2006, MNRAS, 372, 265
 Minchev, I., Chiappini, C., Martig, M. 2012, arXiv1208.1506
 Mishenina, T. V., Korotin, S. A., Klochkova, V. G., Panchuk, V. E. 2000, A&A, 353, 978
 Mishenina, T.V., Kovtyukh, V.V. 2001, A&A, 370, 951
 Mishenina, T.V., Soubiran, C., Kovtyukh, V.V., Korotin, S.A. 2004, A&A, 418, 551
 Mishenina, T. V., Bienaymé, O., Gorbaneva, T. I. et al. 2006, A&A, 456, 1109
 Mishenina, T.V., Soubiran C., Kovtyukh V. V., et al., 2008, A&A, 489, 923
 Mowlavi, N., Eggenberger, P., Meynet, G., et al. 2012, A&A, 541, 41
 Neves, V., Santos, N.C., Sousa, S.G., Correia, A.C.M., & Israeli, G. 2009, A&A, 497, 563
 Nikityuk, T., & Mishenina, T. 2006, A&A, 456, 969
 Nishimura, S., Kotake, K., Hashimoto, M., et al. 2006, ApJ, 642, 410
 Nissen P.E., & Schuster W.J. 2008, Proc. IAU Symposium, 254, 103
 Pakhomov, Yu.V., Antipova, & L.I., Boyarchuk, A.A. 2011, Astr. Rep. 55, 256
 del Peloso, E.F., da Silva, L., & Porto de Mello, G.F. 2005, A&A, 434, 285
 Pignatari, M., Gallino, R., Heil, M., et al. 2010, ApJ, 710, 1557
 Pignatari, M., Gallino, R., Meynet, G., et al. 2008, ApJ, 687, 95
 Prochaska, J.X., Naumov, S.O., Carney, B.W., McWilliam, A., & Wolfe, A.M. 2000, AJ, 120, 2513
 Qian, Y.-Z., Wasserburg, G.J. 2008, ApJ, 687, 272
 Rauscher, T., Heger, A., Hoffman, R. D., Woosley, S. E. 2002, ApJ, 576, 323
 Reddy, B.E., Lambert, D.L., & Allende Prieto, C. 2006, MNRAS, 367, 1329
 Rutten R.J. 1978, SoPh 56, 237
 Schoening, T., Butler, K., 1998, A&AS, 128, 581
 Serminato A., Gallino R., Travaglio C., Bisterzo S., Straniero O. 2009, PASA, 26, 153
 Sobelman I.I., Vainshtein L.A., Yukov E., 1981, Excitation of Atoms and Broadening of Spectral Lines, Springer Ser. in Chem. Phys., Berlin, Springer
 Soubiran, & C., Girard, F. 2005, A&A, 438, 139
 Soubiran, C., Bienaymé, O., Mishenina, T. V.,& Kovtyukh, V. V. 2008, A&A, 480, 91
 Sneden, C., 2008, Bull. AAS, 40, 264

- Steinmetz, M., Zwitter, T., Siebert, A. et al. 2006, AJ, 132, 1645
 Straniero, O., Dominguez, I., Imbriani, G., & Piersanti, L. 2003, ApJ, 583, 878
 Surman, R., McLaughlin, G. C., Ruffert, M., Janka, H.-Th., & Hix, W. R. ApJ, 679, L117
 The, L-S, El Eid, M. F., & Meyer, B. S. 2007, ApJ, 655, 1058
 Thielemann, F.-K., Nomoto, K., & Yokoi, K. 1986, A&A, 158, 17
 Thielemann, F.-K., Brachwitz, F., Hoflich, P., Martinez-Pinedo, G., & Nomoto, K. 2004, New A Rev., 48, 605
 Thielemann, F.-K., Arcones, A., Kappeli, R., et al. 2011, Progress in Particle and Nuclear Physics, 66, 346
 Timmes, F. X., Woosley, S. E., & Weaver, T. A. 1995, ApJS, 98, 617
 Timmes, F.X., Brown, E.F., & Truran, J.W. 2003, ApJ, 590, 83
 Tolstoy, E., Hill, V., Tosi, M. 2009, ARA&A, 47, 371
 Travaglio, C., Gallino, R., Arnone, E., Cowan, J., Jordan, F., & Sneden, C. 2004, ApJ, 601, 864
 Travaglio, C., Hillebrandt, W., & Reinecke, M. 2005, A&A, 443, 1007
 Travaglio, C., Ropke, F. K., Gallino, R., & Hillebrandt, W. 2011, ApJ, 739, 93
 Truran, J. W., Cowan, J. J., Pilachowski, C. A., & Sneden, Ch. 2002, PASP, 114, 1293
 Tsymbal, V.V. 1996, ASP Conf. Ser. 108, 198
 van Regemorter, H., 1962, ApJ, 136, 906
 Winteler, C., Kappeli, R., Perego, A., et al. 2012, ApJ, 750, 22
 Woosley, S.E., Wilson, J.R., Mathews, G.J., Hoffman, R.D., & Meyer, B.S. 1994, ApJ, 433, 229

Table 4. The stellar parameters and α -element and Ni abundances in studied stars

HD	Teff	log g	[Fe/H]	Probab	[O/Fe]	[Mg/Fe]	[Si/Fe]	[Ca/Fe]	[Ni/Fe]
Thick									
HD	Teff	log g	[Fe/H]	Probab	[O/Fe]	[Mg/Fe]	[Si/Fe]	[Ca/Fe]	[Ni/Fe]
HD000245	5400	3.40	-0.84	0.95	0.33	0.32	0.29	0.38	-0.02
HD003765	5079	4.30	0.01	0.9		0.02	0.09	0.06	0.04
HD005351	4378	4.60	-0.21	0.95	0.14	0.09	0.22		0.07
HD006582	5240	4.30	-0.94	0.69	0.51	0.37	0.32	0.32	0.00
HD013783	5350	4.10	-0.75	0.72		0.41	0.30	0.25	0.02
HD018757	5741	4.30	-0.25	0.92	0.08	0.35	0.06	0.19	0.03
HD022879	5972	4.50	-0.77	0.93	0.48	0.42	0.28	0.25	0.02
HD065583	5373	4.60	-0.67	0.96	0.48	0.22	0.26	0.20	0.10
HD076932	5840	4.00	-0.95	0.89	0.51	0.38	0.33	0.38	0.03
HD106516	6165	4.40	-0.72	0.96	0.50	0.25	0.35	0.36	0.07
HD110897	5925	4.20	-0.45	0.62		0.25	0.10	0.06	-0.01
HD135204	5413	4.00	-0.16	0.97		0.23	0.13	0.18	0.00
HD152391	5495	4.30	-0.08	0.95	0.07	0.06	0.04	0.04	0.01
HD157089	5785	4.00	-0.56	0.79	0.41	0.29	0.24	0.23	-0.03
HD157214	5820	4.50	-0.29	0.97		0.13	0.14	0.21	-0.01
HD159062	5414	4.30	-0.40	0.57		0.28	0.22	0.17	0.06
HD165401	5877	4.30	-0.36	0.97		0.26	0.19	0.15	0.05
HD190360	5606	4.40	0.12	0.63		0.06	0.13	-0.02	0.10
HD201889	5600	4.10	-0.85	0.93		0.40	0.33	0.40	-0.02
HD201891	5850	4.40	-0.96	0.89	0.40	0.29	0.32	0.18	-0.03
HD204521	5809	4.60	-0.66	0.6		0.27	0.20	0.15	0.04
Thin									
HD	Teff	log g	[Fe/H]	Probab	[O/Fe]	[Mg/Fe]	[Si/Fe]	[Ca/Fe]	[Ni/Fe]
HD000166	5514	4.60	0.16	0.99	-0.23	-0.13	-0.02	0.03	0.02
HD001562	5828	4.00	-0.32	0.98	0.16	0.18	0.07	0.23	-0.02
HD001835	5790	4.50	0.13	0.99	-0.07	0.00	0.07	0.02	0.03
HD003651	5277	4.50	0.15	0.98	-0.32	-0.02	0.05	0.01	0.11
HD004256	5020	4.30	0.08	0.9	-0.25	0.08	0.17	0.12	0.16
HD004307	5889	4.00	-0.18	0.99	0.17	0.06	0.05	0.06	0.00
HD004614	5965	4.40	-0.24	0.99	0.33	0.10	0.09	0.02	0.02
HD005294	5779	4.10	-0.17	0.99	-0.02	0.08	0.02	0.11	-0.03
HD006660	4759	4.60	0.08	0.92	-0.11	-0.02	0.14	0.06	0.05
HD007590	5962	4.40	-0.10	0.99	-0.07	0.06	0.05	0.22	-0.06
HD007924	5165	4.40	-0.22	0.99	0.10	0.18	0.09	0.07	0.01
HD008648	5790	4.20	0.12	0.99	-0.07	0.00	0.10	0.02	0.09
HD009407	5666	4.45	0.05	0.99		0.01	0.05	0.03	0.05
HD009826	6074	4.00	0.10	0.98	-0.15	0.09	0.15	0.04	-0.01
HD010086	5696	4.30	0.13	0.98	-0.13	-0.02	-0.02	0.05	0.00
HD010307	5881	4.30	0.02	0.92	-0.03	0.06	0.05	-0.02	0.06
HD010476	5242	4.30	-0.05	0.98	0.00	0.03	0.08	-0.02	-0.01
HD010780	5407	4.30	0.04	0.99	-0.13	0.04	-0.01	-0.02	0.03
HD011007	5980	4.00	-0.20	0.96	0.16	0.10	0.06	0.07	0.00
HD011373	4783	4.65	0.08	0.99		-0.13	0.11	-0.04	0.03
HD012846	5766	4.50	-0.24	0.99	0.07	0.14	0.08	0.08	0.00
HD013507	5714	4.50	-0.02	0.99	0.06	-0.05	0.05	0.01	-0.02
HD014374	5449	4.30	-0.09	0.99	0.05	0.07	0.08	0.08	0.01
HD016160	4829	4.60	-0.16	0.94	-0.01	0.12		0.11	
HD017674	5909	4.00	-0.14	0.99	0.15	0.11	0.06	0.08	-0.03
HD017925	5225	4.30	-0.04	0.99	-0.06	0.04	0.05	0.10	0.03
HD018632	5104	4.40	0.06	0.98	-0.18	0.01	0.09	0.12	0.05
HD018803	5665	4.55	0.14	0.99	-0.26	-0.04	0.01	-0.02	0.04
HD019019	6063	4.00	-0.17	0.99	0.05	0.15	0.05	0.17	-0.11
HD019373	5963	4.20	0.06	0.96	-0.06	-0.03	0.08	-0.01	0.06
HD020630	5709	4.50	0.08	0.99	-0.08	-0.12	-0.02	0.04	-0.03
HD022049	5084	4.40	-0.15	0.99	0.04	0.03	0.10	0.07	0.00
HD022484	6037	4.10	-0.03	0.95	0.14	0.02	0.05		-0.01
HD022556	6155	4.20	-0.17	0.99	0.14	0.07	0.12	0.03	0.03
HD024053	5723	4.40	0.04	0.99	-0.03	-0.01	0.07	-0.01	-0.04

Table 4. continued.

HD	Teff	log g	[Fe/H]	Probab	[O/Fe]	[Mg/Fe]	[Si/Fe]	[Ca/Fe]	[Ni/Fe]
HD024238	4996	4.30	-0.46	0.98	0.42	0.26	0.25	0.19	0.09
HD024496	5536	4.30	-0.13	0.98	-0.14	0.14	0.10	0.12	-0.03
HD025665	4967	4.70	0.01	0.98	-0.01	-0.08	0.04	-0.02	0.08
HD025680	5843	4.50	0.05	0.99	0.01	-0.07	0.00	0.08	-0.02
HD026923	5920	4.40	-0.03	0.99	0.11	0.11	-0.02	0.10	-0.05
HD028005	5980	4.20	0.23	0.97	-0.27	0.15	0.12	-0.05	0.10
HD028447	5639	4.00	-0.09	0.99	0.07	0.07	0.10	0.01	0.04
HD029150	5733	4.30	0.00	0.99		0.09	0.05	0.00	0.00
HD029310	5852	4.20	0.08	0.98	-0.03	0.00	0.09	0.05	-0.02
HD029645	6009	4.00	0.14	0.97	-0.09	0.03	0.08	-0.03	0.06
HD030495	5820	4.40	-0.05	0.99	0.09	0.06	0.07	0.04	-0.01
HD033632	6072	4.30	-0.24	0.99	0.24	0.12	0.07	0.06	-0.05
HD034411	5890	4.20	0.10	0.7	0.07	-0.01	0.07	-0.03	0.03
HD037008	5016	4.40	-0.41	0.89	0.24	0.16	0.28	0.18	0.10
HD037394	5296	4.50	0.09	0.98	-0.21	-0.04	-0.03	0.02	-0.01
HD038858	5776	4.30	-0.23	0.97	0.16	0.11	0.04	0.10	0.01
HD039587	5955	4.30	-0.03	0.99		0.07	0.06	0.02	-0.07
HD040616	5881	4.00	-0.22	0.97		0.05	0.02	0.08	-0.03
HD041330	5904	4.10	-0.18	0.96	0.22	0.04	0.08	0.06	-0.01
HD041593	5312	4.30	-0.04	0.99	0.03	-0.08	0.05	0.05	-0.03
HD042618	5787	4.50	-0.07	0.98	0.07	0.07	0.03	0.04	-0.01
HD042807	5719	4.40	-0.03	0.98	0.03	0.03	-0.01	0.07	-0.05
HD043587	5927	4.10	-0.11	0.99	0.09	0.08	0.08	0.07	0.06
HD043856	6143	4.10	-0.19	0.99		0.07	0.08	0.08	0.00
HD043947	6001	4.30	-0.24	0.99	0.23	0.12	0.08	0.06	-0.03
HD045088	4959	4.30	-0.21	0.99		0.14	0.15	0.18	0.06
HD047752	4613	4.60	-0.05	0.98	0.05	-0.09	0.14	-0.10	0.09
HD048682	5989	4.10	0.05	0.99		0.03	0.08	0.10	-0.02
HD050281	4712	3.90	-0.20	0.99	0.15	-0.02	0.11	0.14	-0.06
HD050692	5911	4.50	-0.10	0.99	0.10	0.07	0.01	0.06	-0.01
HD051419	5746	4.10	-0.37	0.99	0.30	0.15	0.08	0.12	-0.01
HD051866	4934	4.40	0.00	0.63		0.08	0.09	0.02	0.07
HD053927	4860	4.64	-0.22	0.97		-0.02	0.09		0.06
HD054371	5670	4.20	0.06	0.99	-0.06	0.07	-0.05	0.09	-0.02
HD055575	5949	4.30	-0.31	0.94		0.21	0.10	0.05	0.01
HD058595	5707	4.30	-0.31	0.99	0.16	0.07	0.05	0.12	0.00
HD059747	5126	4.40	-0.04	0.99		0.05	0.05	0.06	-0.0
HD061606	4956	4.40	-0.12	0.99	0.04	-0.10	0.08	0.01	-0.04
HD062613	5541	4.40	-0.10	0.97	0.08	0.07	0.04	-0.01	0.02
HD063433	5693	4.35	-0.06	0.99	0.10	0.02	0.02	0.07	-0.05
HD064468	5014	4.20	0.00	0.94		0.10	0.13	0.17	0.08
HD064815	5864	4.00	-0.33	0.78	0.01	0.31	0.22	0.25	0.04
HD065874	5936	4.00	0.05	0.99	0.01	0.09	0.08	0.05	0.06
HD066573	5821	4.60	-0.53	0.97		0.23	0.24	0.19	0.08
HD068638	5430	4.40	-0.24	0.96	0.18	0.05	0.07	0.10	-0.02
HD070923	5986	4.20	0.06	0.96	0.03	0.07	0.09	-0.01	0.07
HD071148	5850	4.20	0.00	0.92		0.03	0.05	0.00	0.01
HD072760	5349	4.10	0.01	0.99	0.05	0.02	-0.01	0.07	-0.06
HD072905	5884	4.40	-0.07	0.99	0.01	0.09	0.04	0.07	-0.04
HD073344	6060	4.10	0.08	0.98		0.08	0.10	0.08	0.03
HD073667	4884	4.40	-0.58	0.96	0.46	0.26	0.27	0.18	0.06
HD075732	5373	4.30	0.25	0.99	-0.12	0.12	0.10	0.04	0.10
HD075767	5823	4.20	-0.01	0.99	-0.11	0.11	0.00	0.08	-0.04
HD076151	5776	4.40	0.05	0.99		0.06	0.09	-0.01	0.05
HD079969	4825	4.40	-0.05	0.95		0.01	0.07	0.00	0.00
HD082106	4827	4.10	-0.11	0.99	0.02	-0.03	0.05	0.07	-0.03
HD082443	5334	4.40	-0.03	0.99	0.09	-0.02	0.01	0.11	-0.06
HD087883	5015	4.40	0.00	0.99	0.08	0.03	0.12	0.07	0.10
HD088072	5778	4.30	0.00	0.98	-0.21	-0.05	0.09	-0.01	0.03
HD089251	5886	4.00	-0.12	0.99		0.05	0.07	0.06	0.03
HD089269	5674	4.40	-0.23	0.98	0.21	0.13	0.09	0.05	0.03

Table 4. continued.

HD	Teff	log g	[Fe/H]	Probab	[O/Fe]	[Mg/Fe]	[Si/Fe]	[Ca/Fe]	[Ni/Fe]
HD091347	5931	4.40	-0.43	0.98		0.14	0.15	0.06	0.05
HD094765	5077	4.40	-0.01	0.99	0.04	0.06	0.05	0.05	0.03
HD095128	5887	4.30	0.01	0.99	-0.07	0.07	0.05	-0.01	0.03
HD097334	5869	4.40	0.06	0.98	-0.23	-0.01	0.04	0.10	-0.03
HD097658	5136	4.50	-0.32	0.99	0.25	0.08	0.13	0.01	0.03
HD098630	6060	4.00	0.22	0.98	-0.14	0.09	0.16	0.01	0.12
HD101177	5932	4.10	-0.16	0.9	0.21	0.06	0.04	0.09	-0.07
HD102870	6055	4.00	0.13	0.99	-0.03	0.08	0.07	-0.02	0.04
HD105631	5416	4.40	0.16	0.98	-0.28	-0.06	-0.02	0.02	0.05
HD107705	6040	4.20	0.06	0.99	-0.04	-0.10	0.09	0.00	0.01
HD108954	6037	4.40	-0.12	0.99	0.10	0.09	0.07	0.06	-0.01
HD109358	5897	4.20	-0.18	0.99	0.11	0.09	0.05	0.06	0.02
HD110463	4950	4.50	-0.05	0.99	-0.02	0.03	0.00	0.13	-0.07
HD110833	5075	4.30	0.00	0.99	-0.01	-0.04	0.10	0.02	0.05
HD111395	5648	4.60	0.10	0.99		-0.01	0.01	0.03	0.00
HD112758	5203	4.20	-0.56	0.85	0.43	0.19	0.23	0.22	0.07
HD114710	5954	4.30	0.07	0.99	-0.05	-0.07	0.05	-0.05	-0.02
HD115383	6012	4.30	0.11	0.99	-0.03	0.04	0.10	0.06	0.02
HD115675	4745	4.45	0.02	0.9		-0.05	0.14	0.12	0.13
HD116443	4976	3.90	-0.48	0.98	0.32	0.06	0.16	0.14	-0.03
HD116956	5386	4.55	0.08	0.99	-0.31	-0.11	0.04	0.05	0.01
HD117043	5610	4.50	0.21	0.93	-0.15	0.02	0.04	-0.08	0.13
HD119802	4763	4.00	-0.05	0.99		-0.04	0.07	0.09	-0.06
HD122064	4937	4.50	0.07	0.99	0.06	0.01	0.14	-0.06	0.09
HD124642	4722	4.65	0.02	0.99	0.05	-0.12	0.16	-0.01	0.03
HD125184	5695	4.30	0.31	0.96	-0.30	-0.05	0.01	-0.11	0.10
HD126053	5728	4.20	-0.32	0.96	0.19	0.17	0.12	0.08	-0.02
HD127506	4542	4.60	-0.08	0.96		-0.07	0.08		0.03
HD128311	4960	4.40	0.03	0.99		-0.01	0.11	0.01	0.05
HD130307	4990	4.30	-0.25	0.98	0.02	0.08	0.05	-0.02	-0.06
HD130948	5943	4.40	-0.05	0.99	0.14	0.02	0.04	0.09	-0.08
HD131977	4683	3.70	-0.24	0.98	0.15	0.12	0.18	0.19	0.03
HD135599	5257	4.30	-0.12	0.99	0.08	0.00	0.05	0.04	-0.01
HD137107	6037	4.30	0.00	0.98	0.00	0.05	0.06	0.06	-0.05
HD139777	5771	4.40	0.01	0.98		-0.01	0.05	0.11	-0.02
HD139813	5408	4.50	0.00	0.98		0.01	0.09	0.09	-0.04
HD140538	5675	4.50	0.02	0.99	0.06	-0.02	0.05	0.09	0.05
HD141004	5884	4.10	-0.02	0.91		0.10	0.08	0.02	0.03
HD141272	5311	4.40	-0.06	0.97		0.04	0.07	0.05	-0.02
HD142267	5856	4.50	-0.37	0.96	0.25	0.10	0.05	0.07	0.14
HD144287	5414	4.50	-0.15	0.94		0.07	0.12	0.10	0.00
HD145675	5406	4.50	0.32	0.99	-0.14	0.06	0.09	-0.04	0.13
HD146233	5799	4.40	0.01	0.99	-0.12	0.04	0.05	-0.08	0.03
HD149661	5294	4.50	-0.04	0.99	0.06	0.02	0.09	0.05	0.05
HD149806	5352	4.55	0.25	0.99	-0.25	-0.14	0.07	-0.02	0.02
HD151541	5368	4.20	-0.22	0.98	0.23	0.05	0.03	0.07	-0.06
HD153525	4810	4.70	-0.04	0.99	0.11	-0.08	0.08		0.08
HD154345	5503	4.30	-0.21	0.91		0.07	0.10	0.12	0.00
HD156668	4850	4.20	-0.07	0.98	-0.05	0.08	0.22	0.06	0.05
HD156985	4790	4.60	-0.18	0.99		0.05	0.20		0.07
HD158633	5290	4.20	-0.49	0.66		0.17	0.15	0.11	0.00
HD160346	4983	4.30	-0.10	0.99	0.10	-0.01	0.09	0.11	0.00
HD161098	5617	4.30	-0.27	0.86	0.24	0.07	0.09	0.12	-0.02
HD164922	5392	4.30	0.04	0.88	-0.01	0.08	0.11	0.12	0.07
HD165173	5505	4.30	-0.05	0.99	0.06	0.13	0.10	0.10	0.04
HD165341	5314	4.30	-0.08	0.99	0.02	0.03	0.10	0.15	0.03
HD165476	5845	4.10	-0.06	0.94	0.05	0.01	0.04	0.00	-0.04
HD165670	6178	4.00	-0.10	0.99	0.07	-0.03	0.11	0.07	0.01
HD165908	5925	4.10	-0.60	0.99	0.29	0.16	0.10	0.20	-0.06
HD166620	5035	4.00	-0.22	0.98	0.13	0.13	0.13	0.24	0.00
HD171314	4608	4.65	0.07	0.98	-0.16	-0.11	0.11	0.00	0.08

Table 4. continued.

HD	Teff	log g	[Fe/H]	Probab	[O/Fe]	[Mg/Fe]	[Si/Fe]	[Ca/Fe]	[Ni/Fe]
HD174080	4764	4.55	0.04	0.98	-0.04	-0.07	0.01	0.18	-0.11
HD175742	5030	4.50	-0.03	0.98		-0.12	0.01	0.06	-0.04
HD176377	5901	4.40	-0.17	0.97		0.04	0.18	0.04	0.17
HD176841	5841	4.30	0.23	0.98	-0.10	0.07		-0.02	
HD178428	5695	4.40	0.14	0.99	-0.26	-0.06	-0.05	-0.01	0.03
HD180161	5473	4.50	0.18	0.97	-0.35	-0.10	0.02	0.02	0.08
HD182488	5435	4.40	0.07	0.99	0.01	0.05	0.10	0.03	0.09
HD183341	5911	4.30	-0.01	0.88	-0.05	0.07	0.09	0.03	0.01
HD184385	5536	4.45	0.12	0.99	-0.12	-0.07	0.00	0.02	-0.04
HD185144	5271	4.20	-0.33	0.94	0.30	0.01	0.06	0.09	-0.04
HD185414	5818	4.30	-0.04	0.99	-0.05	0.05	0.08	0.02	0.04
HD186408	5803	4.20	0.09	0.98		0.09	0.06	0.02	0.03
HD186427	5752	4.20	0.02	0.98		0.09	0.07	-0.06	0.05
HD187897	5887	4.30	0.08	0.99		0.05	0.08	-0.05	0.02
HD189087	5341	4.40	-0.12	0.99	0.14	0.02	0.11	0.01	0.00
HD189733	5076	4.40	-0.03	0.99	-0.19	0.02	-0.01	0.06	0.03
HD190007	4724	4.50	0.16	0.99	-0.16	-0.11	0.10	0.13	0.03
HD190406	5905	4.30	0.05	0.98	-0.12	-0.02	0.02	0.09	0.03
HD190470	5130	4.30	0.11	0.99		0.00	0.03	-0.04	-0.04
HD190771	5766	4.30	0.13	0.99		-0.07	0.14	0.04	0.06
HD191533	6167	3.80	-0.10	0.97	0.08	0.03	0.09	0.12	-0.03
HD191785	5205	4.20	-0.12	0.62	0.15	0.31	0.07	0.15	0.06
HD195005	6075	4.20	-0.06	0.99	0.12	0.12	0.08	0.11	-0.07
HD195104	6103	4.30	-0.19	0.99	0.21	0.16	0.07	0.10	-0.09
HD197076	5821	4.30	-0.17	0.98	0.16	0.07	0.09	0.11	0.01
HD199960	5878	4.20	0.23	0.98	-0.44	0.02	0.10	0.02	0.11
HD200560	5039	4.40	0.06	0.98		-0.03	0.12	0.07	0.09
HD202108	5712	4.20	-0.21	0.99	0.15	0.06	0.05	0.02	-0.05
HD202575	4667	4.60	-0.03	0.99	0.06	-0.07	0.04		-0.02
HD203235	6071	4.10	0.05	0.98		0.10	0.11	0.06	-0.01
HD205702	6020	4.20	0.01	0.98	0.03	0.10	0.08	0.11	0.06
HD206860	5927	4.60	-0.07	0.99		-0.08	0.02	0.06	-0.03
HD208038	4982	4.40	-0.08	0.99	-0.19	-0.04	0.05	0.01	0.01
HD208313	5055	4.30	-0.05	0.98	-0.02	0.10	0.20	0.04	0.04
HD208906	5965	4.20	-0.80	0.98		0.23	0.25	0.15	0.04
HD210667	5461	4.50	0.15	0.98	-0.31	-0.10	0.06	0.01	0.07
HD210752	6014	4.60	-0.53	0.68		0.07	0.11	0.07	0.02
HD211472	5319	4.40	-0.04	0.99	-0.07	0.00	0.05	0.00	-0.01
HD214683	4747	4.60	-0.46	0.99		0.02	0.17		0.09
HD216259	4833	4.60	-0.55	0.99		0.32	0.04		0.03
HD216520	5119	4.40	-0.17	0.99	0.20	0.09	0.01	0.02	-0.07
HD217014	5778	4.20	0.14	0.97		0.06	0.08	-0.06	0.09
HD217813	5845	4.30	0.03	0.99	-0.30	-0.01	0.04	-0.01	0.09
HD218868	5534	4.60	0.25	0.97	-0.37	-0.10	0.13	-0.04	0.06
HD219538	5114	4.40	-0.09	0.99	0.09	0.03	0.09	0.06	-0.01
HD219623	5949	4.20	0.04	0.97		-0.05	0.11	0.07	-0.07
HD220140	5144	4.60	-0.03	0.99		-0.18	0.03	0.16	-0.02
HD220182	5364	4.50	-0.03	0.98	0.03	0.05	0.01	0.05	0.08
HD220221	4868	4.50	0.16	0.99	-0.22	-0.08	0.12	0.05	0.02
HD221851	5184	4.40	-0.09	0.98	0.07	0.10	0.02	0.07	-0.04
HD222143	5781	4.30	0.09	0.99	-0.09	-0.03	0.04	0.09	0.05
HD224465	5745	4.50	0.08	0.98	-0.05	-0.05	0.24	0.04	0.02
HD263175	4734	4.50	-0.16	0.78	0.04	0.02	0.08		0.06
BD+01 2063	4859	4.40	-0.22	0.99	0.10	0.00	0.15	-0.02	0.13
BD+12 4499	4678	4.70	0.00	0.97	0.03	-0.12		0.04	-0.01
Hercules									
HD013403	5724	4.00	-0.31	0.65	0.28	0.10	0.06	-0.11	0.00
HD019308	5844	4.30	0.08	0.67	0.04	0.00	0.09	0.09	0.03
HD023050	5929	4.40	-0.36	0.76	0.33	0.21	0.18	-0.23	0.03
HD030562	5859	4.00	0.18	0.85	-0.11	0.03	0.06	0.24	0.08
HD064606	5250	4.20	-0.91	0.85		0.37	0.27	-0.57	0.03

Table 4. continued.

HD	Teff	log g	[Fe/H]	Probab	[O/Fe]	[Mg/Fe]	[Si/Fe]	[Ca/Fe]	[Ni/Fe]
HD068017	5651	4.20	-0.42	0.77	0.35	0.31	0.21	-0.23	0.05
HD081809	5782	4.00	-0.28	0.58	0.28	0.16	0.22	-0.18	0.08
HD107213	6156	4.10	0.07	0.78		0.14	0.14	0.19	0.02
HD139323	5204	4.60	0.19	0.81		0.05	0.09	0.25	0.01
HD139341	5242	4.60	0.21	0.75		-0.02	0.04	0.19	0.12
HD144579	5294	4.10	-0.70	0.84		0.37	0.28	-0.39	0.05
HD159222	5834	4.30	0.06	0.71		0.00	0.08	0.13	0.03
HD159909	5749	4.10	0.06	0.88		0.06	0.07	0.07	0.01
HD215704	5418	4.20	0.07	0.71		0.04	0.06	0.06	0.05
HD218209	5705	4.50	-0.43	0.81	0.22	0.19	0.18	-0.35	0.04
HD221354	5242	4.10	-0.06	0.89	0.09	0.31	0.12		0.02
Nonclas									
HD004628	4905	4.60	-0.36		0.36	0.21	0.18	0.07	0.02
HD004635	5103	4.40	0.07		-0.34	-0.02	0.05	0.01	0.08
HD010145	5673	4.40	-0.01		0.03	0.13	0.07	-0.04	0.05
HD012051	5458	4.55	0.24		-0.41	-0.09	0.00	-0.04	0.06
HD013974	5590	3.80	-0.49		0.21	0.17	0.09	0.19	-0.08
HD017660	4713	4.75	0.17		-0.13	-0.19	0.15	0.11	0.12
HD020165	5145	4.40	-0.08		0.11	0.09	0.10	0.04	0.05
HD024206	5633	4.50	-0.08		0.05	0.05	0.09	-0.05	0.03
HD032147	4945	4.40	0.13		-0.08	-0.06	0.11	0.05	0.03
HD045067	6058	4.00	-0.02		0.01	0.04	0.05	0.03	
HD084035	4808	4.80	0.25		-0.25	-0.22	0.07	0.16	0.00
HD086728	5725	4.30	0.22			-0.11	0.04	0.06	0.05
HD090875	4788	4.50	0.24			-0.14	0.02	0.22	0.14
HD117176	5611	4.00	-0.03		0.08	0.07	0.05	0.02	0.02
HD117635	5230	4.30	-0.46			0.21	0.17	0.19	0.01
HD154931	5910	4.00	-0.10		0.04	0.14	0.08	0.12	0.05
HD159482	5620	4.10	-0.89		0.50	0.37	0.34	0.36	0.02
HD168009	5826	4.10	-0.01			0.03	0.05	0.04	0.02
HD173701	5423	4.40	0.18		-0.09	0.00	0.17	-0.08	0.17
HD182736	5430	3.70	-0.06			0.04	0.01	0.00	0.05
HD184499	5750	4.00	-0.64		0.40	0.37	0.34	0.26	0.07
HD184768	5713	4.20	-0.07		0.11	0.15	0.15	0.03	0.06
HD186104	5753	4.20	0.05			0.06	0.07	0.03	0.04
HD215065	5726	4.00	-0.43			0.00	0.18	0.23	0.03
HD219134	4900	4.20	0.05		-0.26	0.04	0.09	0.01	0.04
HD219396	5733	4.00	-0.10			0.16	0.10	0.10	0.03
HD224930	5300	4.10	-0.91		0.44	0.42	0.29	0.34	0.01

Table 5. n-capture element abundances in studied stars

HD	[Y/Fe]	[Zr/Fe]	[Ba/Fe]	[La/Fe]	[Ce/Fe]	[Nd/Fe]	[Sm/Fe]	[Eu/Fe]
Thick								
HD	[Y/Fe]	[Zr/Fe]	[Ba/Fe]	[La/Fe]	[Ce/Fe]	[Nd/Fe]	[Sm/Fe]	[Eu/Fe]
HD000245	-0.06	0.18	0.02	0.17	-0.03	0.12	0.28	0.35
HD003765	0.06	0.02	-0.09	-0.20	0.06	0.17	-0.05	0.03
HD005351	0.13	0.13	-0.33	0.00	-0.04	0.09	0.05	0.08
HD006582	0.04	0.11	-0.12	0.10	-0.06	0.13	0.19	0.41
HD013783	-0.01	0.06	-0.08	0.11	-0.03	0.20	0.16	0.39
HD018757	-0.14	-0.08	-0.08	-0.11	-0.07	0.07	0.05	0.22
HD022879	0.04	0.25	0.05	0.03	-0.01	0.22	0.14	0.41
HD065583	0.05	0.08	-0.07	-0.09	0.08	0.27	0.34	0.41
HD076932	0.13	0.14	0.10	0.15	-0.01	0.18	0.35	
HD106516	0.06	0.24	0.07	0.09	0.01	0.11	0.22	
HD110897	-0.09	0.00	-0.01	0.01	-0.07	0.09	0.09	0.29
HD135204	-0.05	-0.06	-0.11	-0.12	0.03	0.02	0.05	0.20
HD152391	0.04	-0.07	0.03	-0.18	0.00	0.14	0.13	0.12
HD157089	0.00	0.08	0.02	-0.08	-0.09	0.08	0.16	0.37
HD157214	0.01	0.09	-0.05	0.00	0.04	0.14	0.24	0.21
HD159062	0.11	0.14	0.15	-0.04	0.05	0.20	0.21	0.29
HD165401	-0.14	0.03	-0.12	-0.13	-0.05	0.07	0.27	0.27
HD190360	-0.02	-0.11	-0.06	-0.18	0.12	0.08	0.09	0.02
HD201889	0.15	0.18	0.01	0.02	-0.02	0.10	0.25	0.34
HD201891	-0.06	0.27	-0.06	0.15	-0.05	0.20	0.33	
HD204521	0.04	0.19	-0.06		0.02	0.22	0.32	0.30
Thin								
HD	[Y/Fe]	[Zr/Fe]	[Ba/Fe]	[La/Fe]	[Ce/Fe]	[Nd/Fe]	[Sm/Fe]	[Eu/Fe]
HD000166	-0.05	-0.15	0.12	-0.15	-0.12	0.00	-0.13	-0.09
HD001562	-0.02	-0.06	0.00	-0.02	0.07	0.08	0.07	
HD001835	0.02	-0.08	0.04	-0.12	0.01	-0.11		0.06
HD003651	-0.12	-0.11	-0.14	-0.2	-0.12	-0.09	-0.18	-0.08
HD004256	-0.15	-0.19	-0.16	-0.19	-0.04	-0.04	-0.03	
HD004307	-0.07	-0.07	0.08	0.03	-0.04	0.05	0.06	0.12
HD004614	0.05	-0.02	0.02	-0.06	-0.05	0.07	0.06	0.08
HD005294	-0.04	-0.10	0.15	-0.15	0.02	-0.01	-0.09	0.01
HD006660	-0.10	-0.13	-0.15	-0.12	-0.17	-0.11	-0.09	-0.03
HD007590	-0.10	-0.14	0.11	-0.03	-0.10	0.04	0.01	0.07
HD007924	0.00	0.03	-0.05	-0.01	0.10	0.12	0.06	0.04
HD008648	-0.02	-0.07	-0.04	-0.12	-0.04	-0.13	-0.19	-0.13
HD009407	-0.11	-0.10	-0.02	-0.12	-0.12	-0.06	-0.06	-0.03
HD009826	-0.11		-0.02	-0.27	-0.08		-0.06	
HD010086	-0.18	-0.15	-0.06	-0.09	-0.17	-0.17	-0.18	-0.08
HD010307	0.00	-0.09	-0.02	-0.08	-0.01	-0.13	-0.10	0.12
HD010476	-0.01	-0.07	0.00	-0.02	0.05	0.15	-0.10	-0.06
HD010780	-0.01	0.06	0.09	0.05	0.01	0.05	-0.08	0.05
HD011007	-0.11	0.07	0.05	-0.12	-0.07	0.05	0.03	0.19
HD011373	0.00	0.01	-0.04	-0.01	-0.12	-0.03	-0.01	-0.01
HD012846	-0.11	-0.18	-0.04	-0.08	-0.01	0.05	0.11	0.16
HD013507	0.06	-0.09	0.11	0.02	0.09	0.12	-0.09	0.16
HD014374	0.10	-0.06	0.02	-0.12	0.15	0.05	-0.02	0.13
HD016160	-0.08	-0.07	-0.19	-0.12	-0.11	0.08	-0.08	0.28
HD017674	-0.14	-0.12	-0.03	-0.13	-0.07	-0.01	-0.06	-0.02
HD017925	0.01	-0.07	0.03	-0.08	0.13	0.08	-0.03	0.08
HD018632	-0.13	-0.19	-0.04	-0.18	-0.13	-0.10	-0.09	-0.04
HD018803	-0.16	-0.20	0.00	-0.18	-0.14	-0.13	-0.19	-0.02
HD019019	-0.02	0.03	0.17	-0.14	-0.04	0.07	-0.03	
HD019373	-0.07	-0.08	-0.03	-0.22	-0.05	-0.07	-0.10	0.03
HD020630	-0.12	-0.18	0.07	-0.22	-0.09	-0.06	-0.17	
HD022049	0.04	0.11	0.15	0.01	0.18	0.20	0.14	0.24
HD022484	-0.13	-0.10	0.03	-0.19	-0.02	-0.09	-0.09	0.02
HD022556	0.00	0.05	0.04	-0.07	0.05	0.17	-0.01	0.21
HD024053	0.07	-0.08	0.11	0.00	0.03	0.09	0.08	0.10

Table 5. continued.

HD	[Y/Fe]	[Zr/Fe]	[Ba/Fe]	[La/Fe]	[Ce/Fe]	[Nd/Fe]	[Sm/Fe]	[Eu/Fe]
HD024238	-0.05	-0.04	-0.12	-0.04	-0.08	0.05	0.02	0.18
HD024496	-0.10	-0.19	-0.12	-0.14	-0.02	-0.01	-0.07	0.10
HD025665	-0.17	-0.11	-0.03	-0.09	-0.05	-0.12	-0.15	0.06
HD025680	-0.07	-0.20	0.05	-0.05	-0.11	-0.04	-0.03	0.02
HD026923	-0.05	-0.04	0.28	0.00	-0.12	-0.01	-0.01	0.00
HD028005	0.07	-0.08	0.00	-0.17	-0.03	-0.06	-0.14	-0.13
HD028447	0.03	-0.12	0.03	-0.07	-0.02	0.06	0.02	0.13
HD029150	0.06	-0.10	-0.03	-0.01	-0.03	0.00	-0.01	0.04
HD029310	-0.06	-0.13	0.02		-0.09	-0.17		
HD029645	-0.12	-0.09	-0.07	-0.20	-0.11	-0.17	-0.18	-0.10
HD030495	0.11	0.10	0.19	-0.06	0.07	0.14	0.18	0.07
HD033632	0.09	0.07	0.18	0.10	0.15	0.16	0.16	0.18
HD034411	-0.14	-0.06	-0.01	-0.18	-0.08	-0.17	-0.09	-0.01
HD037008	-0.05	-0.06	-0.24	-0.06	-0.08	0.05	0.03	0.28
HD037394	-0.11	-0.20	0.06	-0.25	-0.11	-0.07	-0.15	-0.02
HD038858	0.01	-0.02	0.03	-0.02	0.05	0.10	0.01	0.15
HD039587	-0.10	-0.01	0.14	-0.03	-0.04	-0.03	0.00	-0.03
HD040616	-0.06	0.04	0.12	-0.07	-0.01	0.11	0.13	-0.04
HD041330	-0.18	0.01	0.01	-0.08	-0.07	0.01	-0.06	0.22
HD041593	0.04	0.01	0.10	0.00	-0.01	0.10	-0.14	-0.07
HD042618	-0.11	-0.18	0.02	-0.04	-0.08	-0.02	-0.01	0.09
HD042807	-0.09	-0.09	0.11	-0.07	-0.07	-0.01	-0.08	0.05
HD043587	-0.12	0.00	-0.04	-0.11	-0.06	-0.05	-0.09	0.15
HD043856	-0.03	-0.08	0.15	-0.03	-0.03	0.03	0.14	0.18
HD043947	0.00	0.02	0.06	0.00	-0.02	0.16	0.07	0.20
HD045088	-0.06	-0.19	0.04	-0.16	-0.07	0.06	-0.03	0.13
HD047752	0.04	0.05	-0.02	0.00	0.01	0.01	-0.01	0.10
HD048682	-0.17	-0.17	-0.08	-0.21	-0.16	-0.18	-0.15	-0.08
HD050281	0.02		0.00	-0.01	0.06	0.12	0.02	
HD050692	-0.08	-0.18	0.03	-0.01	-0.08	-0.01	0.11	0.22
HD051419	-0.05	-0.03	-0.08	-0.10	-0.01	0.07	0.01	0.26
HD051866	-0.14	-0.17	-0.07	-0.15	-0.11	-0.10	-0.13	0.02
HD053927	-0.14	-0.13	-0.02	-0.10	-0.09	-0.03	-0.12	0.19
HD054371	-0.17	-0.18	-0.01	-0.16	-0.16	-0.13	-0.15	0.03
HD055575	-0.07	0.04	0.02	0.06	-0.07	0.14	0.13	0.20
HD058595	0.07	0.02	0.01	0.03	0.18	0.15	0.15	0.20
HD059747	-0.08	-0.14	0.09	-0.10	0.04	0.04	-0.08	0.02
HD061606	0.00		0.02	0.03	0.19	0.15	0.20	0.13
HD062613	0.02	0.01	0.00	0.01	0.02	0.05	0.08	-0.06
HD063433	-0.16	-0.18	0.02	-0.08	-0.09	-0.02	-0.07	0.03
HD064468	-0.19	-0.12	-0.17	-0.14	-0.17	-0.08	-0.13	
HD064815	0.07	0.07	0.07	0.01	0.03	0.17	0.24	0.32
HD065874	0.00	-0.09	-0.07	-0.05	0.01	-0.10	-0.11	-0.11
HD066573	0.10	0.19	-0.07	0.10	0.02	0.14	0.29	0.32
HD068638	0.07	0.02	0.05	0.15	0.18	0.10	0.12	0.08
HD070923	-0.07	-0.09	-0.06	0.07	-0.08	-0.13	-0.07	-0.12
HD071148	-0.02	-0.08	-0.01	0.05	0.03	-0.01	-0.06	-0.06
HD072760	-0.04	-0.01	0.04	0.06	0.00	-0.02	-0.04	0.05
HD072905	0.03	-0.05	0.11	0.05	0.01	-0.01	0.04	0.01
HD073344	-0.08	-0.15	-0.02	0.05	-0.15	-0.16	-0.09	-0.04
HD073667	0.00	0.05	-0.15	0.00	-0.03	0.14	0.17	0.30
HD075732	-0.20	0.00	-0.13	-0.16	-0.01	-0.07	0.04	-0.11
HD075767	-0.13	-0.14	0.04	-0.10	-0.16	-0.10	-0.09	
HD076151	-0.01	-0.07	-0.03	0.13	-0.03	-0.04	-0.12	-0.06
HD079969	-0.15	-0.23		-0.08	-0.16	0.02	-0.14	0.07
HD082106	-0.04		0.11	0.07	0.04	0.10	0.14	-0.05
HD082443	-0.13	-0.20	0.13	-0.04	-0.12	-0.05	-0.08	0.12
HD087883	-0.05	-0.15	-0.05	0.03	-0.01	0.08	-0.05	0.02
HD088072	0.01	0.06	-0.03	0.07	-0.01	0.17	-0.06	0.15
HD089251	0.09	-0.09	0.05	0.12	-0.01	0.02	0.11	0.16
HD089269	0.07	0.08	0.03	0.06	0.10	0.23	0.12	0.20

Table 5. continued.

HD	[Y/Fe]	[Zr/Fe]	[Ba/Fe]	[La/Fe]	[Ce/Fe]	[Nd/Fe]	[Sm/Fe]	[Eu/Fe]
HD091347	-0.07	-0.06	-0.02	-0.01	-0.06	0.09	0.08	0.22
HD094765	-0.02	-0.09	0.07	0.00	0.01	0.06	-0.04	
HD095128	-0.04	0.00	-0.05	-0.04	-0.01	0.05	-0.05	0.00
HD097334	-0.12	-0.17	0.13	-0.08	-0.16	-0.13	-0.13	-0.01
HD097658	-0.12	0.01	-0.03	-0.09	-0.04	0.06	0.05	0.19
HD098630	0.02	-0.18	-0.09	-0.13	-0.05	-0.08	-0.18	-0.10
HD101177	0.02	0.00	0.01	-0.05	0.01	0.06	0.04	0.15
HD102870	-0.07	-0.04	-0.03	-0.10	-0.06	-0.13	-0.15	-0.09
HD105631	-0.18	-0.19	-0.02	-0.19	-0.19	-0.16	-0.18	-0.04
HD107705	-0.05	-0.13	0.06		0.05	-0.13	-0.03	-0.05
HD108954	0.05	0.02	0.11	0.01	0.02	0.10	-0.03	0.06
HD109358	-0.04	0.06	-0.05	-0.07	-0.05	-0.04	0.00	0.04
HD110463	0.05	-0.03	0.04	0.00	0.05	0.16	0.00	0.09
HD110833	0.00	0.02	-0.04	0.01	0.02	0.09	-0.07	
HD111395	-0.04	-0.03	0.19	-0.08	0.04	0.07	0.00	0.02
HD112758	-0.03	0.00	-0.22	0.00	0.05	0.04	0.20	
HD114710	-0.01	-0.06	0.11	0.03	0.05	0.00	-0.01	-0.03
HD115383	0.00	-0.08	0.12	0.00	-0.05	-0.10	-0.01	0.05
HD115675	-0.02	-0.03	-0.07	-0.14	0.01	0.07	-0.04	0.03
HD116443	0.00	-0.03	-0.18	-0.04	0.00	0.10	0.09	0.17
HD116956	-0.08	-0.17	0.05	-0.06	-0.03	-0.02	-0.11	0.04
HD117043	0.03	-0.04	0.10	0.00	0.01	-0.10	-0.01	-0.07
HD119802	-0.06	0.07	0.02	-0.11	0.04	-0.01	-0.04	-0.06
HD122064	-0.19		-0.07	0.07	0.16		0.15	0.07
HD124642	-0.06	-0.06	-0.02	-0.08	-0.09	-0.09	-0.17	0.10
HD125184	0.03	-0.07	0.04	-0.18	0.07	-0.01	-0.05	-0.07
HD126053	0.03	0.04	-0.13	0.12	-0.06	0.09	0.20	0.06
HD127506	-0.07	-0.03	-0.04	-0.06	-0.09	0.03	-0.11	0.08
HD128311	-0.07	0.00	-0.03	-0.06	-0.04	0.02	-0.08	0.04
HD130307	-0.05	-0.04	0.08	-0.02	0.04	0.21	0.04	0.20
HD130948	-0.06	-0.19	0.15	-0.07	-0.12	0.00	-0.14	0.07
HD131977	0.01	0.05	-0.11	-0.1	-0.03	0.12	0.05	0.18
HD135599	0.00	0.08	0.10	0.02	0.06	0.11	0.03	0.11
HD137107	-0.02	0.00	0.09	0.00	0.04	-0.05	-0.18	
HD139777	-0.14	-0.11	0.14	-0.22	-0.12	-0.05	-0.10	-0.09
HD139813	-0.10	-0.20	0.15	-0.17	0.04	-0.03	0.04	0.12
HD140538	-0.02	0.11	0.06	0.05	0.10	0.01	0.01	0.12
HD141004	-0.12	-0.11	0.00	-0.09	-0.06	-0.09	-0.11	0.11
HD141272	-0.18	-0.06	0.14	-0.14	-0.04	0.02	-0.03	0.08
HD142267	-0.12	-0.04	-0.03	0.07	-0.01	0.11	0.24	0.19
HD144287	0.05	-0.06	-0.03	0.15	0.10	0.13	0.05	
HD145675	-0.05	-0.10	-0.09	-0.14	0.03	0.00	-0.07	-0.03
HD146233	-0.02	-0.05	0.01	0.03	-0.02	-0.01	-0.08	0.08
HD149661	-0.07	0.05	0.01	0.05	0.08	0.02	-0.09	0.03
HD149806	-0.18	-0.18	0.05	-0.22	-0.08	-0.11	-0.16	-0.08
HD151541	-0.14	0.02	-0.15	0.01	0.04	0.06	-0.07	0.26
HD153525	-0.05	-0.03	0.04	-0.01	-0.03	0.14	0.06	0.16
HD154345	0.10	-0.04	-0.05	-0.19	0.07	0.04	0.02	0.15
HD156668	-0.12	-0.09	-0.13	-0.07	-0.07	0.05	-0.02	0.05
HD156985	0.08	0.05	-0.09	-0.06	0.08	0.08	0.05	0.20
HD158633	-0.12		-0.16	0.07	0.05	0.17	0.18	0.08
HD160346	-0.06		-0.08	0.05	0.06	0.14	-0.10	0.04
HD161098	-0.05	-0.04	-0.02	0.02	0.00	0.13	0.05	0.26
HD164922	-0.15	0.04	-0.10		0.08	0.03	0.01	0.10
HD165173	-0.13		-0.07		0.09	0.07	0.13	0.09
HD165341	-0.21	0.04	0.03	0.04	0.12	0.17	0.15	0.00
HD165476	-0.07	-0.07	-0.06	-0.02	-0.10	0.00	-0.09	
HD165670	-0.06		0.10	0.06	-0.06	-0.08	0.15	
HD165908	-0.03	0.04	0.04	-0.03	0.03	0.05	0.14	0.14
HD166620	-0.14		-0.09	0.07	0.02	0.00	-0.03	0.16
HD171314	-0.03	-0.04	-0.09	-0.1	-0.14	-0.06	-0.10	0.10

Table 5. continued.

HD	[Y/Fe]	[Zr/Fe]	[Ba/Fe]	[La/Fe]	[Ce/Fe]	[Nd/Fe]	[Sm/Fe]	[Eu/Fe]
HD174080	-0.11	-0.16	-0.01	-0.23	-0.17	-0.13	-0.05	0.13
HD175742	-0.20	-0.14	0.06	-0.08	-0.13	-0.08	-0.09	0.05
HD176377	-0.17	-0.15	0.05	-0.13	-0.09	0.02	0.07	0.14
HD176841	-0.16	-0.10	-0.12	-0.2	-0.09	-0.17	-0.08	-0.09
HD178428	-0.18	-0.19	0.04	-0.17	-0.15	-0.11	-0.16	0.03
HD180161	-0.18	-0.14	0.07	-0.15	-0.15	-0.12	-0.09	-0.01
HD182488	-0.04	0.03	-0.07		0.03	0.07		-0.03
HD183341	0.04	-0.08	-0.08	-0.07	0.03	-0.07	-0.14	0.10
HD184385	-0.18	-0.14	0.07	-0.15	-0.14	-0.15	-0.18	-0.02
HD185144	-0.10		-0.02	-0.02	-0.02	0.10	-0.04	0.17
HD185414	-0.15	-0.09	0.07	-0.07	-0.10	-0.04	-0.08	0.04
HD186408	-0.11	-0.11	-0.03	0.00	-0.01	-0.04	-0.07	-0.05
HD186427	-0.04	-0.03	-0.07	0.00	0.03	-0.07	-0.11	0.02
HD187897	-0.03	-0.05	0.03	-0.02	-0.10	-0.07	0.04	
HD189087	0.08	0.07	0.10	0.09	0.14	0.17	0.06	0.06
HD189733	-0.15	-0.15	-0.11	-0.11	-0.04	0.00	-0.04	0.05
HD190007	-0.06	-0.19	-0.03	-0.18	-0.20	-0.16	-0.15	-0.04
HD190406	-0.16	-0.15	0.05	-0.08	-0.14	-0.09	-0.11	-0.03
HD190470	-0.16	-0.15	-0.08	-0.1	-0.07	-0.07	-0.11	0.01
HD190771	-0.20	-0.20	-0.07	-0.15	-0.19	-0.19	-0.17	-0.06
HD191533	0.01	-0.11	0.09	-0.16	0.14	-0.06	-0.09	-0.06
HD191785	-0.12	-0.10	-0.24	-0.16	-0.11	-0.02	-0.07	0.14
HD195005	-0.09	-0.10	0.06	-0.06	-0.02	-0.12	-0.11	
HD195104	0.10	-0.11	0.20	0.08	0.10	0.23	0.16	0.03
HD197076	0.11	0.12	0.08	0.10	0.08	0.21	0.13	0.21
HD199960	-0.14	-0.12	-0.11	-0.25	-0.04	-0.17	-0.07	
HD200560	-0.03	-0.03	0.04	-0.07	-0.09	-0.04	-0.12	-0.09
HD202108	-0.04	-0.11	0.10	-0.13	-0.02	0.09	-0.09	0.15
HD202575	0.05	-0.04	0.09	-0.04	0.02	0.08	-0.02	0.10
HD203235	-0.14	-0.12	-0.05	-0.05	-0.07	-0.09	-0.11	-0.01
HD205702	0.11	-0.10	-0.03	-0.08	-0.02	-0.04		-0.02
HD206860	-0.12	-0.17	0.05	-0.03	-0.04	0.02	0.05	
HD208038	-0.08	-0.07	0.09	-0.02	-0.06	0.04	-0.04	0.10
HD208313	-0.11	-0.17	-0.09	-0.08	-0.06	0.00	-0.17	-0.03
HD208906	-0.05	0.17	-0.14	-0.09	0.02	0.14	0.11	0.34
HD210667	-0.07	0.02	-0.04	-0.09	-0.01	-0.10	-0.12	-0.01
HD210752	-0.02	0.09	0.03	-0.04	0.01	0.16	0.31	0.37
HD211472	0.05	-0.05	0.10	0.07	0.05	0.06	-0.07	
HD214683	-0.02	-0.01	0.06	0.01	0.05	0.15	0.12	0.28
HD216259	0.10	0.19	-0.10	0.14	0.14	0.18	0.25	0.22
HD216520	-0.13	0.00	-0.20	-0.12	0.00	0.07	0.08	0.09
HD217014	-0.16	-0.09	-0.10	-0.21	-0.03	-0.13	-0.13	-0.05
HD217813	-0.18	-0.17	0.04	-0.10	-0.12	-0.10	-0.14	-0.01
HD218868	-0.10	-0.14	0.03	-0.15	-0.10	-0.10	-0.15	-0.03
HD219538	-0.04	-0.05	-0.06	0.08	0.04	0.11	0.01	0.06
HD219623	-0.17	-0.19	0.01	-0.23	-0.20	-0.18	-0.17	0.13
HD220140	-0.15	-0.11	0.05	0.00	-0.16	-0.09	-0.12	0.00
HD220182	-0.06	-0.20	0.07	-0.10	-0.03	0.04	-0.06	0.10
HD220221	-0.02	-0.06	0.02	-0.03	-0.06	-0.06	-0.04	-0.09
HD221851	-0.07	-0.13	0.02	-0.05	0.01	0.05	-0.07	0.11
HD222143	-0.14	-0.14	0.09	-0.18	-0.15	-0.15	-0.17	-0.02
HD224465	-0.18	-0.12	0.05	-0.07	-0.13	-0.13	-0.19	0.04
HD263175	-0.07	-0.06	-0.13	-0.07	-0.02	0.02	0.03	0.23
BD+01 2063	0.00	-0.02	0.07	-0.09	-0.03	-0.01	-0.02	0.05
BD+12 4499	0.07	-0.03	0.02	0.02	0.01	0.05	-0.07	0.24
Hercules								
HD013403	-0.05	0.10	-0.09	-0.03	-0.02	0.16	0.09	0.15
HD019308	-0.04	-0.05	-0.01	-0.29	-0.04	-0.04	-0.08	-0.04
HD023050	0.09	-0.08	-0.04	0.00	0.08	0.22	0.26	0.25
HD030562	-0.05	-0.03	0.02	-0.09	0.01	-0.02	-0.03	0.02
HD064606	0.01	0.16	-0.14	0.11	-0.06	0.13	0.19	0.40

Table 5. continued.

HD	[Y/Fe]	[Zr/Fe]	[Ba/Fe]	[La/Fe]	[Ce/Fe]	[Nd/Fe]	[Sm/Fe]	[Eu/Fe]
HD068017	-0.07	0.03	-0.12	-0.07	-0.04	0.07	0.14	0.26
HD081809	-0.08	-0.02	-0.15	-0.07	0.07	0.16	0.04	0.17
HD107213	0.02	-0.09	0.02	-0.16	-0.08	-0.11	0.06	
HD139323	0.03	0.04	0.00	-0.10	0.20	0.14	0.15	0.10
HD139341	0.01	0.05	-0.07	-0.20	0.15	0.05	-0.04	0.13
HD144579	-0.16	0.08	-0.25		0.08	0.11	0.15	0.24
HD159222	-0.01	-0.05	-0.03	-0.24	0.05	-0.10	-0.17	-0.07
HD159909	-0.16	-0.11	-0.11	-0.24	-0.08	-0.09	-0.16	0.03
HD215704	-0.20	0.01	-0.12	0.01	-0.04	-0.04	0.04	0.02
HD218209	-0.04	0.01	-0.01	0.09	-0.02	0.15	0.13	0.27
HD221354	-0.17	-0.19	-0.26	-0.24	-0.14	-0.07	-0.10	0.08
Nonclas								
HD004628	0.08	0.09	-0.04	0.03	0.16	0.13	0.24	
HD004635	-0.13	-0.11	-0.04	-0.20	-0.11	-0.10	-0.13	0.00
HD010145	-0.09	-0.11	-0.06	-0.09	0.01	0.12	0.02	0.15
HD012051	-0.17	-0.18	0.10	-0.26	-0.06	-0.13	-0.17	-0.07
HD013974	-0.20	-0.09	-0.01	0.00	-0.11	0.05	0.08	0.01
HD017660	-0.08	-0.12	-0.14	-0.21	-0.20	-0.19	-0.09	0.15
HD020165	-0.08	-0.10	-0.07	-0.09	-0.02	0.11	-0.08	0.00
HD024206	0.07	0.11	0.03	0.05	0.15	0.17	0.13	0.07
HD032147	-0.13		-0.04	-0.02	0.13	0.02	0.12	0.06
HD045067	-0.13	-0.13	0.00	-0.25	-0.02	-0.15	-0.15	-0.04
HD084035	-0.05	-0.07	-0.05	-0.29	-0.05	-0.10	-0.12	-0.08
HD086728	-0.23	-0.26	-0.06	-0.33	-0.19	-0.23	-0.21	-0.10
HD090875	-0.15	-0.19	-0.01	-0.29	-0.18	-0.15	-0.14	
HD117176	-0.09	-0.12	-0.01	-0.02	0.01	0.02	-0.01	0.07
HD117635	0.04	-0.01	-0.04	-0.06	0.09	0.15	0.15	0.30
HD154931	-0.01	-0.04	0.01	-0.16	-0.03	0.01	-0.06	-0.01
HD159482	-0.05	0.12	-0.01	0.06	-0.06	0.06	0.24	0.35
HD168009	-0.19	-0.04	-0.06	-0.26	-0.08	-0.16	-0.14	0.05
HD173701	-0.07	0.02	-0.10	-0.15	-0.06	0.05	-0.07	-0.14
HD182736	-0.05	0.04	0.05	0.00	-0.02	0.05	0.07	
HD184499	-0.11	0.08	-0.10	-0.02	0.00	0.07	0.21	0.37
HD184768	-0.08	-0.06	-0.09	-0.10	0.00	0.06	-0.04	0.11
HD186104	-0.06	-0.13	-0.05	-0.19	-0.11	-0.10	0.00	0.09
HD215065	-0.14	-0.05	-0.16	-0.06	-0.03	0.12	0.19	
HD219134	-0.11		-0.03		0.12	0.11	-0.09	-0.11
HD219396	-0.15		-0.09	-0.06	0.00	0.21	0.05	
HD224930	0.07	0.13	-0.09	0.06	-0.09	0.02	0.24	